J. Fluid Mech. (2014), *vol.* 761, *pp.* 360–398.
doi:10.1017/jfm.2014.641

The dynamics of breaking internal solitary waves on slopes

Robert S. Arthur[1],† **and Oliver B. Fringer**[1]

[1]The Bob and Norma Street Environmental Fluid Mechanics Laboratory, Department of Civil and Environmental Engineering, Stanford University, Stanford, CA 94305, USA

(Received 21 May 2014; revised 20 October 2014; accepted 28 October 2014; first published online 27 November 2014)

Using direct numerical simulations (DNS), we investigate the structure and energetics of breaking internal waves on slopes. We employ a Navier–Stokes code in an idealized three-dimensional domain where an internal solitary wave of depression impinges upon a sloping bottom. Seven cases with varying initial wave amplitude and bathymetric slope, but constant wave Reynolds number Re_w are considered. Volume-integrated values of dissipation and irreversible mixing are related to the density and velocity structure of the wave throughout the breaking process. The majority of dissipation (63 %) occurs along the no-slip bottom boundary. Most of the remaining dissipation (35 %) and nearly all irreversible mixing occurs in the interior after breaking, when density overturns are present at the interface. Breaking introduces three-dimensionality to the flow field that is driven by the lateral breakdown of density overturns and the lobe–cleft instability typical of gravity currents. The resulting longitudinal rolls (streamwise vorticity) increase dissipation by roughly 8 % and decrease irreversible mixing by roughly 20 % when compared with a similar two-dimensional simulation. The bulk mixing efficiency is shown to increase for larger and smaller values of the internal Iribarren number ξ, with a minimum for intermediate values of ξ and a peak near $\xi = 0.8$ for plunging breakers. This trend is explained by the degree of two-dimensionality in the flow, and agrees with previous results in the literature after accounting for Reynolds number effects. Local turbulence quantities are also calculated at 'virtual moorings', and a location upslope of the breakpoint but downslope of the intersection of the pycnocline and the bottom is shown to provide a signal that is most representative of the volume-integrated dissipation and mixing results.

Key words: internal waves, stratified flows, turbulent mixing

1. Introduction

Internal tides are formed in the ocean by the interaction of the barotropic tide with topographic features. As internal tides propagate, they steepen due to nonlinearity and disperse into trains of internal solitary waves. Ultimately, these waves interact with the continental or nearshore slope, where they steepen further and eventually break. Prior to breaking, the dynamics of shoaling internal solitary waves are described well by

† Email address for correspondence: barthur@stanford.edu

the weakly nonlinear, weakly dispersive Korteweg–deVries (KdV) equation (Helfrich & Melville 2006). In shallow water and during and after breaking, however, KdV theory breaks down and non-analytical methods must be used to describe internal wave dynamics.

Although field observations of shoaling and breaking internal waves have been made in the past (Klymak & Moum 2003; Scotti & Pineda 2004; Shroyer, Moum & Nash 2009; Davis & Monismith 2011; Nam & Send 2011; Walter *et al.* 2012, 2014), these results are limited by the spatial and temporal resolution of field data. For this reason, a wide range of numerical and laboratory studies have explored the breaking process of internal solitary waves on slopes in more idealized domains. These studies have examined shoaling and breaking mechanisms, as well as the formation of upslope surges of dense water that are referred to as bores or boluses (Wallace & Wilkinson 1988; Helfrich 1992; Lamb 2002; Vlasenko & Hutter 2002; Venayagamoorthy & Fringer 2007). Of particular interest has been a classification of breaking mechanisms across the full parameter space of incoming wave and slope conditions. Boegman, Ivey & Imberger (2005) created one such classification using the internal Iribarren number

$$\xi = \frac{s}{\sqrt{a/L_w}}, \tag{1.1}$$

where s is the bathymetric slope, a is the wave amplitude and L_w is the solitary wavelength. Aghsaee, Boegman & Lamb (2010) expanded this classification, defining surging, collapsing, plunging and fission breaker types based on several time scales associated with breaking. Including smaller, more realistic slopes $s = O(0.01)$ allowed Aghsaee *et al.* (2010) to capture fission breakers, which were not included in Boegman *et al.*'s (2005) classification. During fission, the rear face of the initial wave separates into a train of solitary waves of elevation that propagate up the slope as boluses. Fission has been observed in the field (Shroyer *et al.* 2009) and with a two-dimensional field-scale numerical model (Bourgault *et al.* 2007*a*).

Much of the interest in internal wave interaction with bottom topography stems from Munk & Wunsch's (1998) claim that turbulence due to breaking internal waves at boundaries accounts for a significant sink of energy in the ocean. In addition, turbulent mixing caused by breaking internal waves has implications for nearshore distributions of temperature, nutrients, and larvae (Pineda 1994; Leichter *et al.* 1996; Omand *et al.* 2011), as well as sediment transport (Bourgault *et al.* 2014) and dissolved oxygen variability (Walter *et al.* 2014). For these reasons, the mixing associated with breaking internal waves on slopes has also been an active area of research. Several studies have quantified the 'mixing efficiency', or the proportion of initial wave energy that contributes to irreversible mixing of the density field. Michallet & Ivey (1999) used laboratory experiments to calculate the mixing efficiency as a function of the ratio between the length scale of the wave and the length scale of the slope. They found that for small values of this ratio (small slopes), breaking is not vigorous and the mixing efficiency is low. For large vales of this ratio (large slopes), the mixing efficiency is again low because most of the incoming energy is reflected off of the slope. The mixing efficiency peaks around 25 % for intermediate values of the ratio, when the most vigorous breaking occurs. Boegman *et al.* (2005) also recast Michallet & Ivey's (1999) results in terms of the internal Iribarren number, and found that the peak mixing efficiency occurs when $\xi \approx 0.8$, corresponding to plunging breakers.

However, Bourgault & Kelley (2007*b*) found that the results of Michallet & Ivey (1999) were likely affected by dissipation due to sidewall friction.

Estimates of the mixing efficiency have also been made for other internal wave-breaking mechanisms. Hult, Troy & Koseff (2011) used novel laboratory techniques to measure the mixing efficiency of internal waves interacting with a bathymetric ridge. Specifically, they separated the mixing efficiency into different regions of the flow, including the interface, where breaking occurs, and the lower layer, where flow interacts with the bottom boundary. They found a local mixing efficiency of 10–17 % at the interface, where wave breaking contributes to turbulent mixing, and no mixing in the lower layer, where boundary-induced turbulence exists but has no density gradients to mix. This resulted in an overall mixing efficiency of 4–7 % for the entire domain. Fringer & Street (2003) used a high-resolution numerical model to calculate the mixing efficiency of breaking internal waves in deep water. Using the formulation of Winters *et al.* (1995), they found a maximum instantaneous mixing efficiency of 0.36 ± 0.02. Using the formulation of Michallet & Ivey (1999), they found a 'bulk' mixing efficiency of 0.42 ± 0.07. Fringer & Street (2003) also provide a summary of mixing efficiency values from previous studies in their table 1. In addition, Fringer & Street (2003) examined the dynamics of the breaking process, and found that progressive internal waves break due to an initial two-dimensional instability (either Kelvin–Helmholtz billows or Rayleigh–Taylor instability) that is uniform in the lateral (cross-stream) direction. These initial instabilities create unstable stratification that leads to a secondary convective instability in the lateral direction. This secondary instability manifests itself in the form of streamwise vorticity, or 'longitudinal rolls' that significantly affect dissipation and mixing in the domain.

Numerical modelling has been used extensively to study shoaling and breaking internal waves on slopes both at the field (Lamb 2002; Bourgault *et al.* 2007*a*; Vlasenko & Stashchuk 2007; Walter *et al.* 2012) and laboratory (Vlasenko & Hutter 2002; Venayagamoorthy & Fringer 2007; Aghsaee *et al.* 2010) scales. While field-scale models are able of capturing realistic wave and slope conditions, they fail to resolve the small-scale processes associated with breaking. Conversely, laboratory-scale models begin to resolve breaking processes but fail to capture realistic wave and slope conditions. Several high-resolution three-dimensional modelling studies have examined turbulence and mixing during internal wave generation and breaking on critical slopes. These include the direct numerical simulations (DNS) of Gayen & Sarkar (2010) and the large-eddy simulations (LES) of Gayen & Sarkar (2011). However, most previous modelling studies of breaking internal waves on slopes have used two-dimensional domains that suppress the three-dimensional variability of the breaking process seen in these studies and in Fringer & Street (2003), thus preventing the accurate calculation of breaking energetics.

The present study uses DNS to examine the dynamics of breaking internal solitary waves on slopes. We capture the three-dimensional structure of wave–slope interaction and breaking, and examine the effects of this structure on dissipation and mixing. Section 2 introduces the governing equations and computational setup, while § 3 describes the general structure and energetics of breaking. We examine the three-dimensional flow features induced by breaking and their effects on wave structure and energetics in § 4. The effects of initial wave amplitude and bathymetric slope are discussed in § 5. Finally, we discuss the geophysical application of our results in § 6.

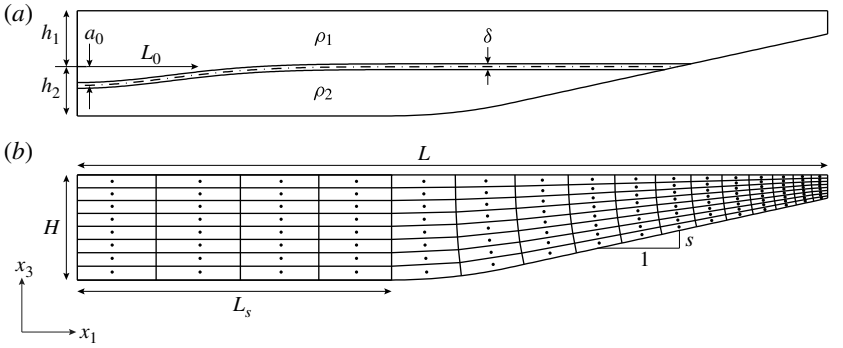

FIGURE 1. The domain used to study breaking internal waves on slopes. (*a*) The initial stratification, where $\rho_1 = 985$ kg m^{-3}, $\rho_2 = 1015$ kg m^{-3} and $\delta = 2$ cm. The parameters a_0, L_w, h_1, and h_2 are shown in table 1. (*b*) The physical dimensions of the domain and a coarse example of the orthogonal curvilinear grid (without vertical stretching). Here, $L_s = 1.675$ m and the lateral (x_2, into the page) width of the domain is $W = 0.1$ m. The parameters L, H, and s are shown in table 1. The radius of curvature of the rounded bottom at the beginning of the slope is 3 m.

2. Governing equations and computational set-up

We solve the Navier–Stokes equations with the Boussinesq approximation given by

$$\frac{\partial u_i}{\partial t} + u_j \frac{\partial u_i}{\partial x_j} = -\frac{1}{\rho_0}\frac{\partial p}{\partial x_j} + \nu \frac{\partial^2 u_i}{\partial x_j \partial x_j} - \frac{g}{\rho_0}\rho \delta_{i3}, \tag{2.1}$$

$$\frac{\partial \rho}{\partial t} + u_j \frac{\partial \rho}{\partial x_j} = \kappa \frac{\partial^2 \rho}{\partial x_j \partial x_j}, \tag{2.2}$$

$$\frac{\partial u_i}{\partial x_i} = 0, \tag{2.3}$$

where ν is the kinematic viscosity and κ is the scalar diffusivity. Here, we use the Einstein summation convention with $i, j, k = 1, 2, 3$ and x_3 as the vertical coordinate. Equations (2.1)–(2.3) are solved using the code Cui (1999) in the three-dimensional domain shown in figure 1. This code is parallelized with MPI and employs the fractional-step method of Zang, Street & Koseff (1994) to solve the momentum and scalar transport equations. The method of Zang *et al.* (1994) has been used extensively in the past to study geophysical flows at the laboratory scale (for a complete list, see Venayagamoorthy & Fringer 2007; Chou & Fringer 2010). Although the code includes the dynamic-mixed model of Zang, Street & Koseff (1993), in the present study we do not use this model, but instead perform DNS.

For all simulations, the initial stratification is given by

$$\frac{\rho}{\rho_0}(x_1, x_3, t = 0) = 1 - \frac{\Delta\rho}{2\rho_0} \tanh\left[\frac{2(x_3 + h_1 + \zeta(x_1))}{\delta} \tanh^{-1}(\alpha)\right] \tag{2.4}$$

where the reference density $\rho_0 = 1000$ kg m^{-3}, the density difference between the top and bottom layer $\Delta\rho = \rho_2 - \rho_1 = 30$ kg m^{-3}, the upper layer depth $h_1 = 0.3$ m, the interface thickness $\delta = 2$ cm and $\alpha = 0.99$. A solitary wave of depression is created

Case	L (m)	H (cm)	h_1, h_2 (cm)	a_0, L_0 (cm)	s	ν (m^2 s^{-1})	δ_S (mm)	ξ	Type
1	4	56	30, 26	5, 70	0.218	2.50×10^{-7}	2.4	1.51	S
2	3.5	56	30, 26	10, 70	0.3	1.00×10^{-6}	4.9	1.47	C
3	4	56	30, 26	10, 70	0.218	1.00×10^{-6}	4.9	1.07	C
4	4	56	30, 26	15, 70	0.218	2.25×10^{-6}	7.3	0.87	P
5	4	56	30, 26	20, 70	0.218	4.00×10^{-6}	9.8	0.76	P
6	5	56	30, 26	10, 70	0.15	1.00×10^{-6}	4.9	0.73	C
7	11	56	30, 26	10, 70	0.05	1.00×10^{-6}	4.9	0.24	F

TABLE 1. The solitary wave cases considered in this study in terms of the domain length L, the domain height H, the upper-layer depth h_1, the lower-layer depth h_2, the amplitude of the initial half-Gaussian a_0, the length scale of the initial half-Gaussian L_0, the bottom slope s, the kinematic viscosity ν, the Stokes' boundary-layer thickness δ_S, the internal Iribarren number ξ and the breaker type (S = surging, C = collapsing, P = plunging, F = fission).

in the domain by initializing the interface with a half-Gaussian at the left boundary (e.g. Fringer 2003; Bourgault *et al.* 2007*a*). This interface ζ is given by

$$\zeta(x_1) = a_0 \exp\left[-\left(\frac{x_1}{L_0}\right)^2\right] + \zeta' R, \tag{2.5}$$

where a_0 and L_0 are the initial amplitude and length scale of the half-Gaussian, respectively. An initial perturbation $\zeta' R$, where $\zeta' = 1$ mm and $R \in \{-1, 1\}$ is a uniformly distributed random number, is also added to the interface to trigger lateral instabilities during breaking.

Seven wave cases are considered here, and summarized in table 1. Following Troy & Koseff (2005), we classify each case in terms of the wave Reynolds number $Re_w = a^2\omega_0/\nu$, where a is the amplitude of the initial solitary wave after it has formed, and was found to be approximately $a_0/2$. The wave frequency ω_0 is estimated as c_0/λ, where $c_0 = \sqrt{g' h_1 h_2/H}$ is the linear phase speed of an internal wave in a two-layer fluid ($g' = g\Delta\rho/\rho_0$ is the reduced gravity) and $\lambda \approx 2L_w$ is the wavelength. The solitary wavelength L_w is calculated as (Michallet & Ivey 1999)

$$L_w = \frac{1}{a}\int_0^{L_s} \eta(x_1)\mathrm{d}x_1, \tag{2.6}$$

where η is the displacement of the $\rho = \rho_0$ isopycnal from h_1. Here, L_w was found to be approximately 1.2 m for all cases. Case 3 is considered the base case with $\nu = 10^{-6}$ m^2 s^{-1} and $Re_w = 208$. To facilitate direct comparison of dissipation and mixing between cases, ν is changed relative to the base case in order to maintain a constant Re_w. The wave Reynolds number is proportional to $(a/\delta_S)^2$, where $\delta_S = \sqrt{2\nu/\omega_0}$ is the Stokes' boundary-layer thickness. Thus, we maintain a constant initial wave amplitude to Stokes' boundary-layer thickness ratio for each case. For all cases, the Prandtl number $Pr = 1$ such that $\kappa = \nu$. Following Aghsaee *et al.* (2010), we also calculate the internal Iribarren number ξ for each case and classify the breaker type, as shown in table 1.

The boundary conditions for all velocity components are no-slip on the bottom wall and free-slip on the top, left and right walls. The density field has a gradient-free

boundary condition on the top, bottom, left and right walls. All variables are periodic in the lateral (x_2) direction. Each simulation was run on an orthogonal curvilinear grid generated using the open-source software gridgen (available online at https://code.google.com/p/gridgen-c/). Cases 1, 3, 4 and 5 were computed on a grid of size $N_1 \times N_2 \times N_3 = 1152 \times 96 \times 128 \approx 14 \times 10^6$ points. To account for different length domains, $N_1 = 1024$ for case 2 ($\approx 13 \times 10^6$ points), $N_1 = 1408$ for case 6 ($\approx 17 \times 10^6$ points) and $N_1 = 2048$ for case 7 ($\approx 25 \times 10^6$ points). Grid stretching of the form $\Delta x_i^k = r\Delta x_i^{k+1}$, where r is the stretching factor and k is the index of the grid point, is employed in the horizontal (x_1) and vertical (x_3) directions to increase resolution in the breaking region. Grid spacing in the lateral (x_2) direction is constant. In the horizontal direction, stretching is applied from $x_1 = 0$ to L_s with $r = 1.01$, concentrating $N_1 - 128$ points (approximately 90 %) into the sloping region. The grid is also stretched slightly in x_1 in the sloping region to maintain orthogonality. In the vertical direction, stretching is performed twice. First, grid points are concentrated toward the bottom with $r = 1.02$ in order to resolve the flow near the wall. Second, 100 of 128 points (78 %) are concentrated in the bottom 35 % of the domain with $r = 1.07$ in order to resolve the interface and lower layer during breaking. The resulting grid resolution at the interface in the breaking region is approximately $\Delta x_1 \times \Delta x_2 \times \Delta x_3 = 4$ mm $\times$ 1 mm $\times$ 2 mm. Near the bottom wall, the vertical coordinate is measured in wall units $x_3^+ = x_3/\delta_S$. The vertical resolution near the wall is therefore $\Delta x_3^+ = \Delta x_3/\delta_S < 1$. In the worst-case scenario, the grid spacing is found to be within approximately one order of magnitude (a factor of 13) of the Kolmogorov length scale η_k (defined in § 4.2). For further discussion of grid resolution, see § 4.2.

A time step of $\Delta t = 0.003$ s was used for all simulations. The number of time steps varied by case, and was 20 000 for cases 1–5, 30 000 for case 6 and 37 000 for case 7. Simulations were run on the US Army Research Lab DoD Supercomputing Research Center (ARL DSRC) supercomputer Harold using 432 processors (cases 1, 3, 4 and 5), 384 processors (case 2), 528 processors (case 6), and 768 processors (case 7). With a computation time of approximately 10 s per time step, this resulted in wall-clock simulation times of 56 h (24 000 CPU hours; cases 1, 3, 4 and 5), 56 h (21 000 CPU hours; case 2), 83 h (44 000 CPU hours; case 6) and 103 h (79 000 CPU hours; case 7).

3. Physical description of breaking

3.1. *Energy definitions*

We define the volume-integrated kinetic and potential energy in the domain as

$$E_k = \frac{1}{2}\int_V u_i u_i \mathrm{d}V, \tag{3.1}$$

$$E_p = \frac{g}{\rho_0}\int_V \rho x_3 \mathrm{d}V, \tag{3.2}$$

where V is the volume of integration, discussed below. Following Winters *et al.* (1995), we split the potential energy into its available (E_a) and background (E_b) components such that

$$E_p = E_a + E_b, \tag{3.3}$$

$$E_b = \frac{g}{\rho_0}\int_V \rho(x_3^*) x_3^* \mathrm{d}V. \tag{3.4}$$

The background potential energy E_b represents the lowest possible potential energy state of the system, if it were to return to rest adiabatically. Its calculation requires $\rho(x_3^*)$, the background density field, which can be found numerically through a sort of the density field $\rho(x_3)$. Here, we employ the parallel Quicksort algorithm of Li *et al.* (1993). Details of the background potential energy calculation in the code can be found in Koltakov & Fringer (2012).

In the absence of boundary fluxes, the background potential energy evolves according to

$$\frac{\mathrm{d}E_b}{\mathrm{d}t} = \phi_d = \frac{\kappa g}{\rho_0}\int_V x_3^* \frac{\partial^2}{\partial x_j \partial x_j}\rho(x_3^*)\mathrm{d}V, \tag{3.5}$$

where ϕ_d is the rate of change of the background potential energy due to irreversible density changes within the domain. The total potential energy evolves according to

$$\frac{\mathrm{d}E_p}{\mathrm{d}t} = \phi_z + \phi_i, \tag{3.6}$$

where $\phi_z = g\int_V \rho u_3 \mathrm{d}V$ is the reversible buoyancy flux and $\phi_i = (\kappa g/\rho_0)\int_A(\rho_{top} - \rho_{bottom})\mathrm{d}A$ is the irreversible change from internal to potential energy. In the definition of ϕ_i, ρ_{top} and ρ_{bottom} are the densities on the top and bottom boundaries of the domain, respectively, and A is the corresponding surface area of the boundary. It follows that

$$\frac{\mathrm{d}E_a}{\mathrm{d}t} = \phi_z - (\phi_d - \phi_i). \tag{3.7}$$

From (3.5), it becomes clear that the background potential energy changes only due to molecular diffusion of the density field, or irreversible diapycnal mixing. Reversible changes in the density field are due to 'stirring' processes. These changes are available for exchange with the kinetic energy field and are contained in ϕ_z. This exchange can be seen in the evolution equation for the kinetic energy,

$$\frac{\mathrm{d}E_k}{\mathrm{d}t} = -\phi_z - \epsilon, \tag{3.8}$$

where the volume-integrated dissipation is defined as

$$\epsilon = \nu\int_V \frac{\partial u_i}{\partial x_j}\frac{\partial u_i}{\partial x_j}\mathrm{d}V. \tag{3.9}$$

Finally, the total energy in the domain E_T evolves according to

$$\frac{\mathrm{d}E_T}{\mathrm{d}t} = \frac{\mathrm{d}E_p}{\mathrm{d}t} + \frac{\mathrm{d}E_k}{\mathrm{d}t} = -\epsilon + \phi_i. \tag{3.10}$$

For energy quantities E and their rates of change $\mathrm{d}E/\mathrm{d}t$ (specifically, those shown in figure 3*a*,*b* respectively), the volume of integration V is chosen as the entire computational domain in order to capture the evolution of the solitary wave over the full simulation. However, for irreversible energy quantities ϵ, ϕ_d and ϕ_i, V is restricted to the sloping region of the domain ($x_1 > L_s$; see figure 4) to eliminate effects that occur prior to shoaling and breaking. We note that in the calculation of ϕ_d, the background density field $\rho(x_3^*)$ is still calculated for the entire domain, but only integrated over the sloping region. Thus, ϕ_d may be thought of as the contribution of the sloping region to the total irreversible mixing in the domain.

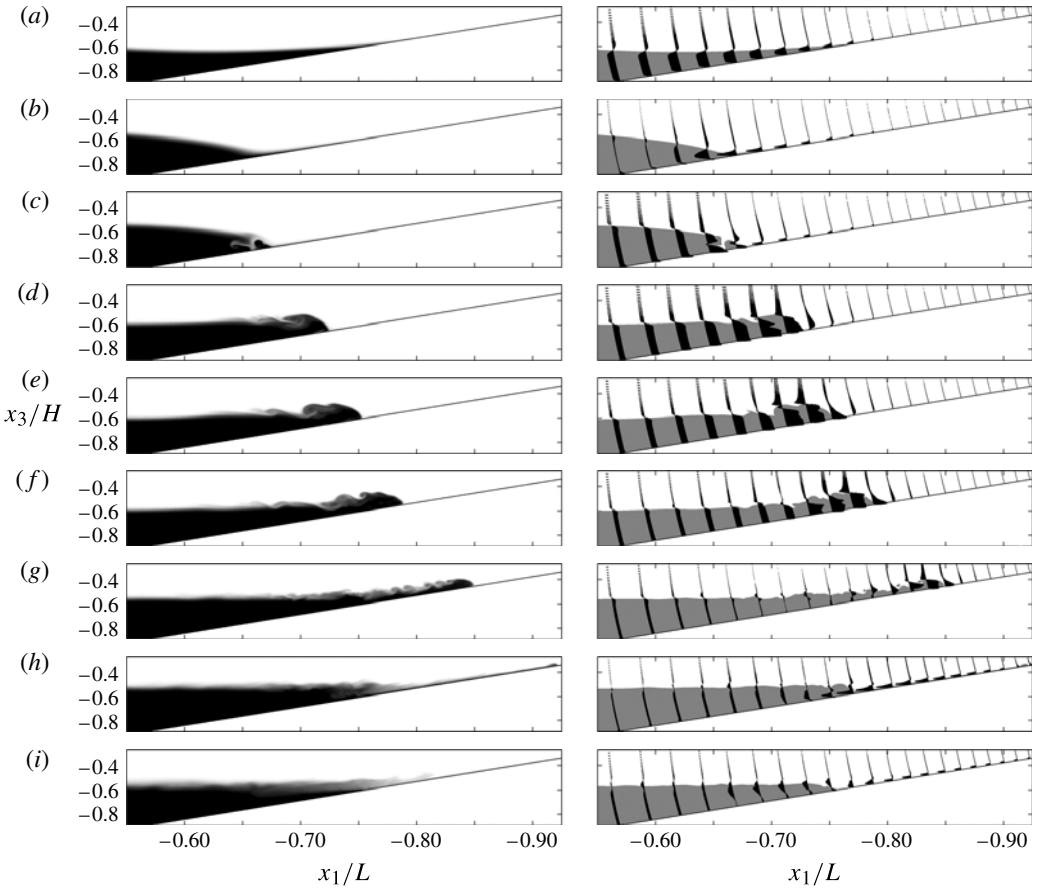

FIGURE 2. Snapshots in time of density structure (left column) and velocity structure (right column) for breaking wave case 3. Results are averaged in the lateral (x_2) direction. In the left column, black corresponds to $\rho = \rho_0 + \Delta\rho/2$ and white corresponds to $\rho = \rho_0 - \Delta\rho/2$. The lower layer ($\rho > \rho_0$) is shown in grey the right column as well. Dots labelled a–i in figures 3, 5, 14, 15 and 23–25 correspond to the labels shown here.

In what follows, we present normalized values of the above energetics quantities. Specifically, energy quantities E have the initial value E_0 removed and are then normalized by the absolute value of the minimum available potential energy $|E_{a,min}|$. Rates of energy change $\mathrm{d}E/\mathrm{d}t$ are normalized by the absolute value of the minimum rate of change of available potential energy $|(\mathrm{d}E_a/\mathrm{d}t)_{min}|$. The minimum absolute value is used in both cases because $E_{a,min} < 0$ and $(\mathrm{d}E_a/\mathrm{d}t)_{min} < 0$. All other energy flux quantities are normalized by the maximum dissipation ϵ_{max} for the given case. Time is normalized in all figures by the wave period $T = 2\pi/\omega_0 \approx 76$ s.

3.2. *General structure and energetics*

We begin with a physical description of the wave-breaking process in terms of density and velocity structure (figure 2) and energetics (figure 3). This description is based on the results of case 3, but is representative of the results for all cases. Initially, a solitary wave of depression forms and propagates toward the slope. As the leading

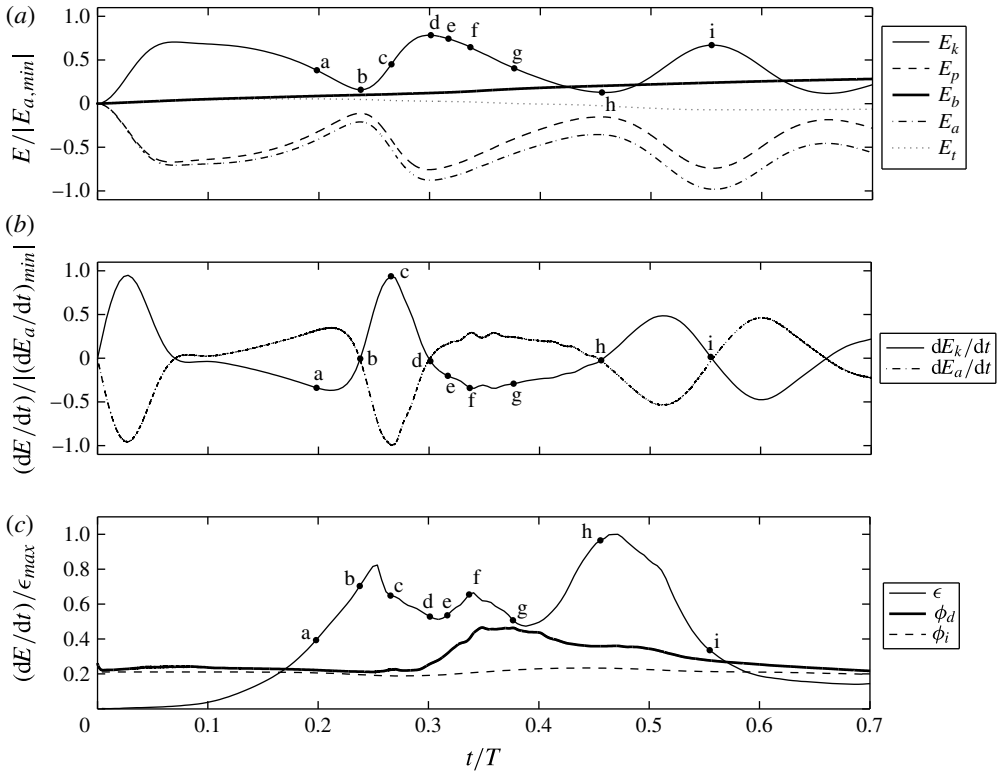

FIGURE 3. Volume-integrated energy results for breaking wave case 3. (*a*) Energy quantities E_k, E_p, E_b, E_a and E_t, all normalized by $|E_{a,min}|$. (*b*) Reversible energy evolution quantities $\mathrm{d}E_k/\mathrm{d}t$ and $\mathrm{d}E_a/\mathrm{d}t$, both normalized by $|(\mathrm{d}E_a/\mathrm{d}t)_{min}|$. (*c*) Irreversible energy evolution quantities ϵ, ϕ_d, and ϕ_i normalized by ϵ_{max}. Dots labelled a–i correspond to time snapshots from figure 2.

face of the wave moves over the slope, downslope velocities in the lower layer are concentrated in the thin region between the bottom and the interface (figure 2*a*). Simultaneously, the rear face of the wave steepens because the upslope velocity under the rear shoulder of the wave is proportional to the local height of the lower layer (figure 2*b*). Ultimately, the downslope velocity under the trough and the upslope velocity under the rear face interact, causing the shear that leads to the breaking event (figure 2*c*). After breaking, dense water surges up the slope in the form of a bore or bolus (figure 2*d–h*). Once this surge reaches its maximum upslope location, it then recedes back down the slope (figure 2*i*).

The energetics of the wave are closely related to its structure. This can be seen in figure 3, where the labelled dots correspond to the snapshots shown in figure 2. Initially, the wave gains kinetic energy at the expense of available potential energy as it forms and propagates toward the slope (figure 3*a*, point a). Available potential (kinetic) energy then increases (decreases) as the wave steepens and reaches a maximum (minimum) at the breakpoint (figure 3*a*, point b). During the breaking event, kinetic energy again rises at the expense of available potential energy until the upslope surge begins (figure 3*a*, points b–d). The upslope surge leads to an increase in available potential energy at the expense of kinetic energy until the dense water

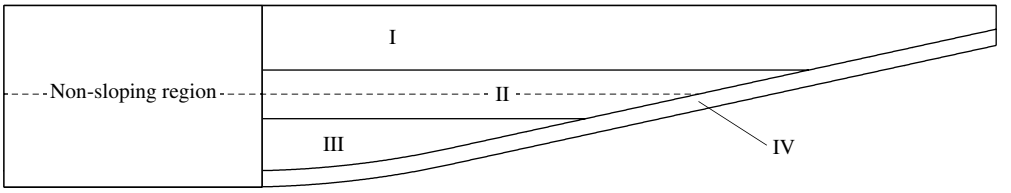

FIGURE 4. Regions used for dissipation calculations. Region I is the upper layer, where $\rho < \rho_0 - 0.99\Delta\rho/2$. Region II is the interior, where $\rho_0 - 0.99\Delta\rho/2 \leqslant \rho \leqslant \rho_0 + 0.99\Delta\rho/2$ (the dashed line shows the location of the initial density interface). Region III is the lower layer, where $\rho > \rho_0 + 0.99\Delta\rho/2$. Region IV is the BBL, where $x_3 < -d + \delta_S$ in the breaking region and d is the local depth of the bottom boundary. The non-sloping region is not included in dissipation calculations. Note that regions are not shown to scale and that the boundaries of regions I, II and III move with the flow while region IV is fixed in time.

reaches its maximum upslope location (figure 3*a*, points d–h). Then, the dense water recedes back downslope, gaining kinetic energy at the expense of available potential energy (figure 3*a*, points h–i). Throughout the wave propagation and breaking event, $\mathrm{d}E_k/\mathrm{d}t$ and $\mathrm{d}E_a/\mathrm{d}t$ nearly mirror each other (figure 3*b*), owing to the exchange of energy through the reversible buoyancy flux ϕ_z.

Dissipation and irreversible mixing, shown in figure 3(*c*), result in an imperfect exchange between kinetic and available potential energy. Dissipation ϵ begins as the wave interacts with the slope and is sustained throughout the breaking event, with several peaks. The first peak occurs during the strong downslope flow prior to the breakpoint (figure 3*c*, point b). The second peak occurs after breaking as the surge of dense water forms and propagates upslope (figure 3*c*, point f). The third peak occurs as dense water from the upslope surge recedes back downslope (figure 3*c*, point h). Irreversible mixing occurs throughout the simulation, but is only elevated above the background value after breaking occurs. We therefore define an effective mixing rate

$$\phi_e = \phi_d - \phi_i, \tag{3.11}$$

as the rate of mixing above the background value.

The effects of dissipation and irreversible mixing are apparent in the background potential energy and total energy profiles (figure 3*a*). The background potential energy increases monotonically throughout the simulation, but increases at a faster rate after breaking (after approximately $t/T = 0.25$) due to elevated mixing. This increase in background potential energy accounts for the separation between the available potential energy and potential energy curves. The total energy in the system initially increases due to background mixing. However, it ultimately decreases as the effect of mixing is overwhelmed by that of dissipation.

3.3. *Interior and bottom boundary energetics*

In order to understand the sources of dissipation in the domain, we separate the total dissipation ϵ into four regions, as shown in figure 4. Therefore,

$$\epsilon = \epsilon_I + \epsilon_{II} + \epsilon_{III} + \epsilon_{IV}, \tag{3.12}$$

where ϵ_I is the dissipation in the upper layer, ϵ_{II} is the dissipation in the interior, ϵ_{III} is the dissipation in the lower layer and ϵ_{IV} is the dissipation in the bottom

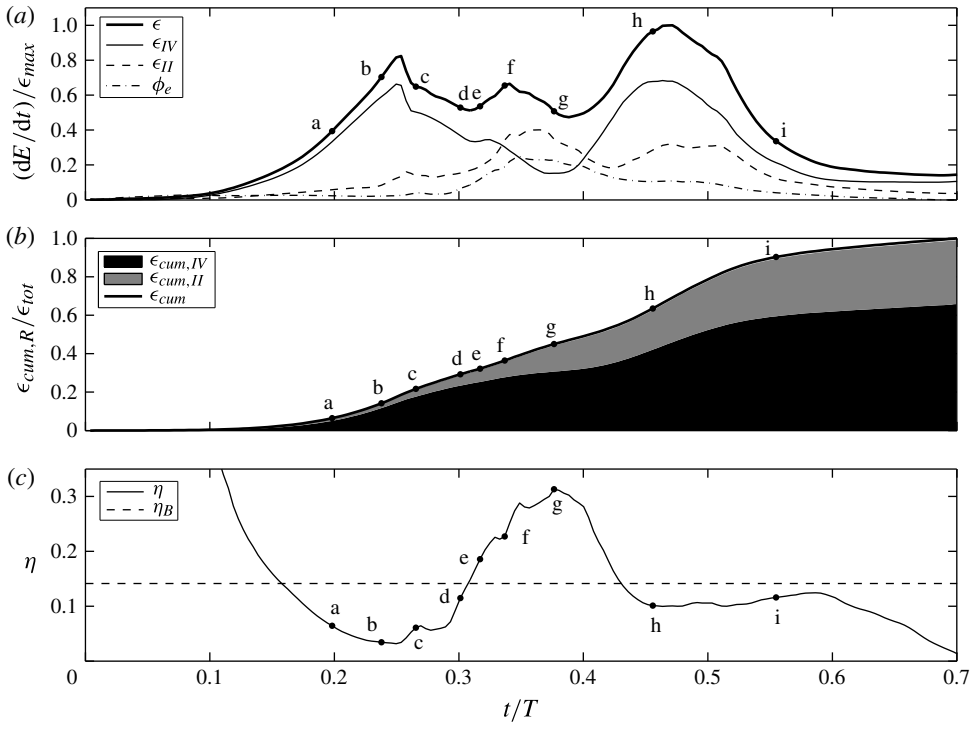

FIGURE 5. Dissipation breakdown by region and mixing efficiency for breaking wave case 3. (*a*) Total dissipation ϵ, bottom-boundary dissipation ϵ_{IV}, interior dissipation ϵ_{II}, and effective irreversible mixing ϕ_e as a function of time, all normalized by ϵ_{max}. (*b*) The cumulative dissipation in the bottom boundary region $\epsilon_{cum,IV}$ and in the interior region $\epsilon_{cum,II}$. The total cumulative dissipation ϵ_{cum} is shown as well. Values are normalized by ϵ_{tot}. (*c*) The instantaneous mixing efficiency η and bulk mixing efficiency η_B. Dots labelled a–i correspond to time snapshots from figure 2.

boundary layer (BBL). The upper layer (region I) is defined as the region above the density interface where $\rho < \rho_0 - 0.99\Delta\rho/2$, and the lower layer (region III) is defined as the region below the density interface where $\rho > \rho_0 + 0.99\Delta\rho/2$. The interior (region II) is defined as the region around the density interface where $\rho_0 - 0.99\Delta\rho/2 \leqslant \rho \leqslant \rho_0 + 0.99\Delta\rho/2$. The bottom boundary region (region IV) is defined as a fixed number of grid cells above the bottom wall. This number was chosen such that $x_3 < -d + \delta_S$ in the breaking region, where d is the local depth of the bottom boundary. Figure 5 shows the dissipation in these regions, both instantaneously (figure 5*a*) and cumulatively (figure 5*b*). The cumulative dissipation, or the total energy lost to dissipation up to time t, is defined as

$$\epsilon_{cum,R} = \int_0^t \epsilon_R \mathrm{d}t, \tag{3.13}$$

where R is the region. The total energy lost to dissipation over the course of the simulation is therefore

$$\epsilon_{tot} = \int_0^{t_{max}} \epsilon \mathrm{d}t. \tag{3.14}$$

The dissipation in the upper and lower layer regions are not shown in figure 5 because they contribute negligibly to the total dissipation.

The first and third peaks in the total dissipation in figure 5(*a*) correspond to peaks in the bottom-boundary dissipation. As discussed in § 3.2, these peaks are associated with the strong downslope flow of dense water in a thin region between the interface and the bottom (figure 5*a*, points b and h, respectively). The second peak in the total dissipation corresponds to the peak in interior dissipation as well as the peak in irreversible mixing. These peaks occur after breaking when dense water surges upslope, suggesting that they are due to the billows that form at the interface during this time (figure 5*a*, points d–g). The third peak in total dissipation also corresponds with a smaller peak in interior dissipation and slightly elevated mixing (figure 5*a*, points h,i). This is associated with the interaction of the downslope flow of dense water from the initial surge interacting with upslope flow under the next wave crest (figure 2*h*,*i*). Cumulatively, dissipation at the bottom boundary accounts for roughly 67 % of the total dissipation in the domain, while dissipation in the interior accounts for roughly 33 % for case 3. Furthermore, the relative contribution of interior dissipation to total dissipation increases after the breakpoint (figure 5*b*, point b).

We do not separate irreversible mixing into the regions shown in figure 4 because ϕ_d is defined as a volume-integrated quantity. Although $\partial^2\rho(x_3^*)/\partial x_j\partial x_j$ in (3.5) can be positive or negative, ϕ_d is guaranteed to be positive (Winters *et al.* 1995). Breaking up the vertical portion $\partial^2\rho(x_3^*)/\partial x_3^2$ of $\partial^2\rho(x_3^*)/\partial x_j\partial x_j$, however, allows ϕ_d to be negative because density gradients may be arbitrarily cut off by region boundaries. Horizontal separation of the domain into the sloping region (where energetics are calculated) and non-sloping region is allowable in this case because horizontal gradients are negligibly affected by this cutoff. In fact, the value of ϕ_d calculated when integrating over both the sloping and non-sloping regions (not shown) is essentially the same as ϕ_d calculated over the sloping region alone. Separating irreversible mixing into the regions in figure 4 using the current method would require sorting the density field separately in each region. Alternatively, Scotti & White (2014) provide a local measure of mixing, based on a local definition of the available potential energy, that would allow for isolated calculations of mixing in arbitrary regions. A full analysis using this method is a topic of future work.

3.4. *Mixing efficiency*

There are two major energy pathways for a breaking internal wave, both of which result in irreversible energy loss. The initial energy of the wave is either (i) exchanged between kinetic energy and available potential energy and ultimately lost to dissipation, or (ii) converted to background potential energy through diffusion of the density field. Dissipation and irreversible mixing, therefore, act as the only possible sinks of initial wave energy. The mixing efficiency measures their relative magnitudes. Winters *et al.* (1995) define the instantaneous mixing efficiency as the instantaneous fraction of irreversible energy exchange that goes into mixing of the density field. Here, we calculate this quantity as

$$\eta = \frac{\phi_e}{\phi_e + \epsilon}. \tag{3.15}$$

Similarly to Michallet & Ivey (1999) and Fringer & Street (2003), we also account for the cumulative effects of dissipation and mixing by calculating the bulk

mixing efficiency

$$\eta_B = \frac{\int_0^{t_{max}} \phi_e \mathrm{d}t}{\int_0^{t_{max}} (\phi_e + \epsilon)\mathrm{d}t} = \frac{\phi_{e,tot}}{\phi_{e,tot} + \epsilon_{tot}}, \tag{3.16}$$

where $\phi_{e,tot}$ is defined in the same way as ϵ_{tot} in (3.14).

The mixing efficiency results for case 3 are shown in figure 5(*c*). The instantaneous mixing efficiency decreases prior to breaking (figure 5*c*, point a) and reaches a minimum at the breakpoint (figure 5*c*, point b). This decrease corresponds to the first peak in dissipation that is caused by strong downslope flow under the leading edge of the wave. The instantaneous mixing efficiency then begins to increase after breaking, and reaches its peak of 0.31 during the upslope surge of dense water (figure 5*c*, points c–g). This corresponds to the increase and peak in irreversible mixing. As the dense water reaches its maximum upslope location and begins to recede (figure 5*c*, points h–i), the instantaneous mixing efficiency decreases again and levels out around the bulk value of 0.14. This decrease corresponds to the third peak in dissipation that is caused by downslope flow of dense water near the bottom. Note that we are not concerned with the instantaneous mixing efficiency near the beginning of the simulation, when a lack of dissipation causes its value to approach unity. This phenomenon was also observed by Smyth & Winters (2003) during the preturbulent phase of breaking Holmboe waves and Kelvin–Helmholtz instabilities.

We acknowledge that the domain-integrated definitions of the mixing efficiency used here combine a variety of dissipation and mixing mechanisms, such as boundary-layer and free shear flow, into one value. In addition, our definitions fail to separate the mean and turbulent components of dissipation and mixing, which undoubtedly contribute to the bulk mixing efficiency in differing amounts. A local definition of mixing efficiency, such as that provided by Scotti & White (2014), would allow for this separation. However, we choose to use the domain-integrated definition here in order to facilitate comparison with previous work, such as that of Fringer & Street (2003), and particularly Michallet & Ivey (1999) and Boegman *et al.* (2005) (see § 5.2).

4. Three-dimensional dynamics

4.1. *Lateral variability*

Internal wave breaking introduces three-dimensionality to the flow field. This three-dimensionality manifests itself in the form of lateral (cross-stream) variability, and is an important component of the structure and energetics discussed above (Fringer & Street 2003). Figure 6 depicts the three-dimensional evolution of the flow over the course of a breaking event, displaying isosurfaces of density ($\rho = \rho_0$) and longitudinal vorticity ω_1. The density structure is initially two-dimensional (figure 6*a*), and remains two-dimensional until after breaking has occurred (figure 6*b*,*c*). Lateral variability is then evident at two distinct locations within the domain: (i) in the interior within a density overturn and (ii) near the bottom at the 'nose' of the upslope surge (figure 6*d*,*e*). Although they appear in different locations, both of these instabilities occur in regions of unstable stratification. A more detailed view of this lateral variability is shown in figure 7.

In the interior, strong shear at the interface leads to billows that are initially two-dimensional. However, since the billows create unstable stratification, they are

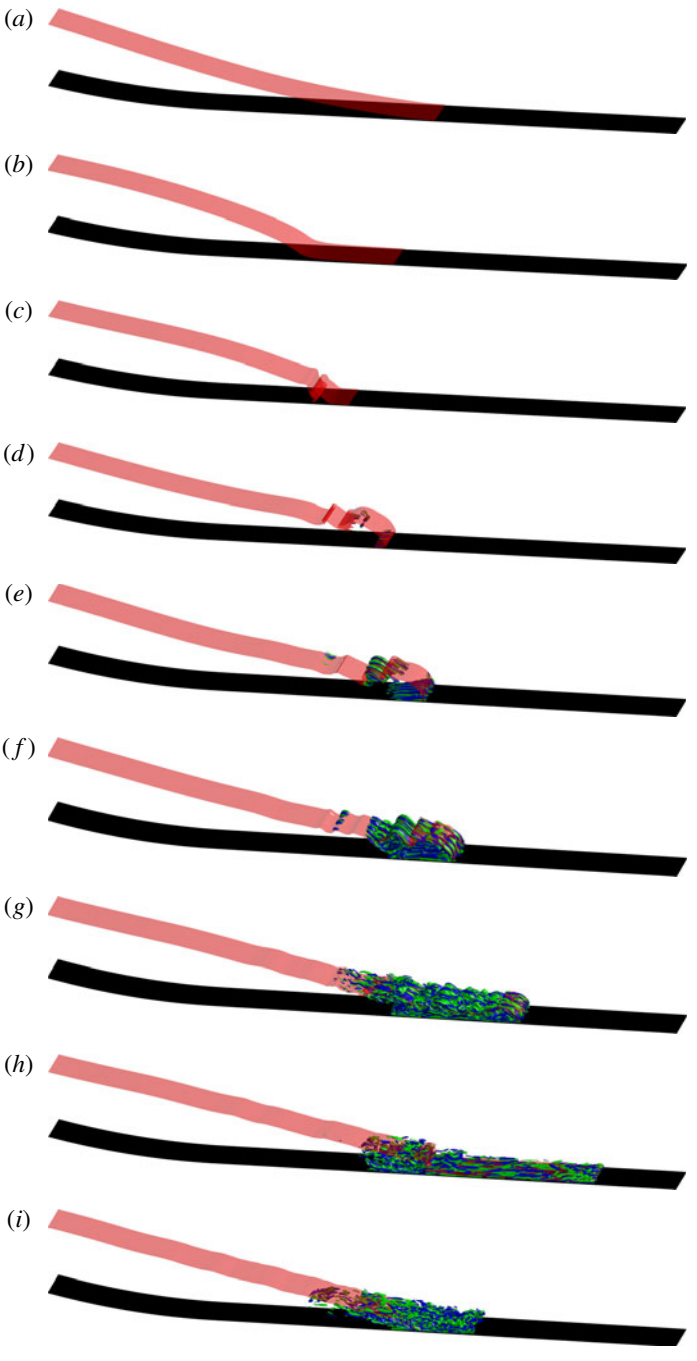

FIGURE 6. Snapshots in time of the three-dimensional structure of breaking wave case 3. Isosurfaces of $\rho = \rho_0$ (red), $\omega_1/\omega_0 = 27$ (blue), and $\omega_1/\omega_0 = -27$ (green) are shown. Blue and green isosurfaces of streamwise vorticity ω_1/ω_0 represent longitudinal rolls. Labels (*a–i*) correspond to the same times as in figure 2.

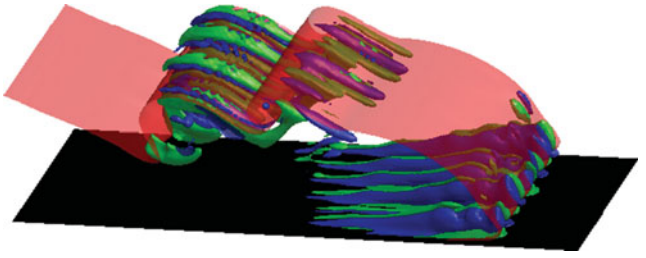

FIGURE 7. A zoomed-in view of figure 6(*e*) showing the development of lateral variability during breaking.

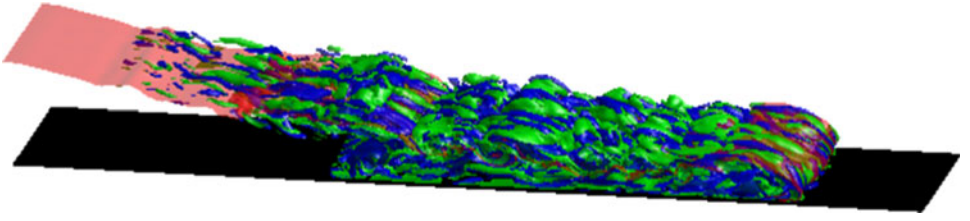

FIGURE 8. A zoomed-in view of figure 6(*g*) showing vortex interaction during the upslope surge.

susceptible to cross-stream convective instability. Specifically, dense fluid sinks and less-dense fluid rises, creating cross-stream plumes within the billow. These plumes generate streamwise vorticity ω_1, as illustrated in figure 9(*a*), which shows an x_2–x_3 slice through the billow in figures 6(*e*) and 7 (see figure 13*e* for the location of the slice). This mechanism of streamwise vorticity generation is the same as that discussed by Fringer & Street (2003) for breaking internal waves in deep water and Winters & D'Asaro (1994) and Dörnbrack (1998) for critical layers. Unstable stratification is also created at the bottom boundary by the no-slip condition; the dense nose of the upslope surge is raised above the bottom, allowing less dense water to flow underneath. Again, cross-stream plumes develop as dense fluid sinks and less dense fluid rises, generating streamwise vorticity ω_1. Figure 9(*b*) depicts these plumes in an x_2–x_3 slice through the nose of the upslope surge in figures 6(*e*) and 7 (see figure 13*e* for the location of the slice). The plumes are visible in three dimensions as 'lobes and clefts', an instability that is typical of gravity currents and was first studied by Simpson (1972). More recently, Härtel, Carlsson & Thunblom (2000) used a linear-stability analysis to examine the lobe and cleft instability mechanism and predict the wavelength of the most unstable mode. Following Fringer & Street (2003), we will refer to the streamwise vortex tubes created by cross-stream instabilities as longitudinal rolls.

Ultimately, the longitudinal rolls from both sources interact. As the upslope surge continues, more longitudinal rolls develop within billows at the interface, and are stretched and tilted by the mean (laterally-averaged) flow. The rolls under the nose experience similar stretching and tilting until vortices from the two sources interact (figure 6*f*,*g*). This interaction, of which a more detailed view is shown in figure 8, is indicative of turbulence and corresponds to elevated interior dissipation and mixing in the domain (figure 5, points f–g). As the upslope surge continues, the longitudinal rolls are dissipated (figure 6*h*,*i*). The growth and decay of turbulence is shown in

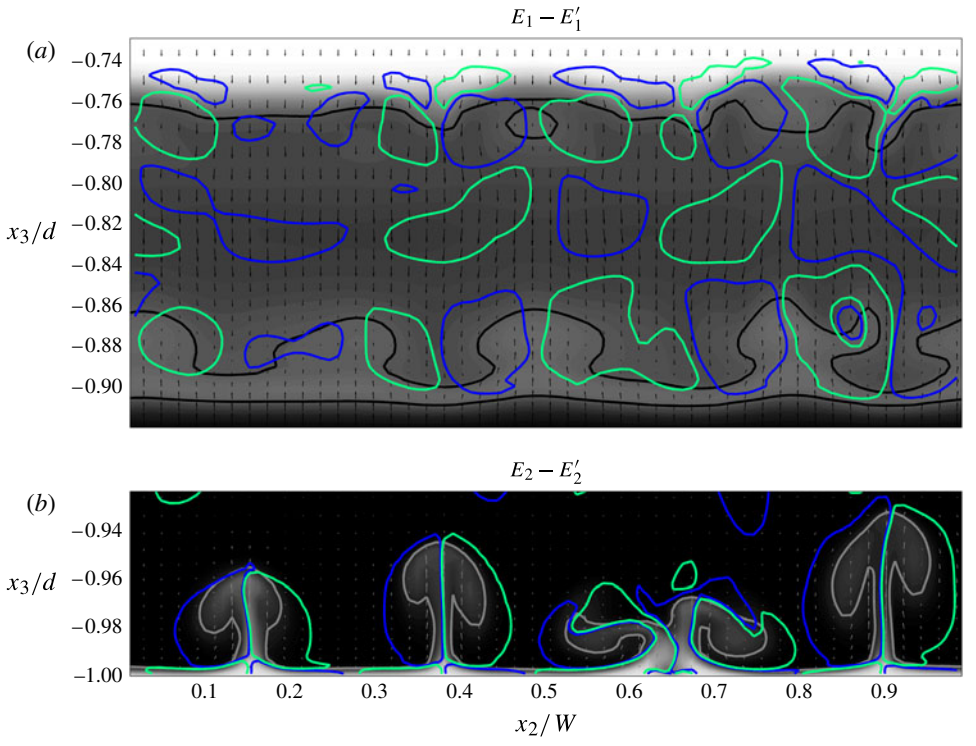

FIGURE 9. An x_2–x_3 slice through the billow (*a*) and nose of the upslope surge (*b*) in figure 6(*e*). Slice locations are shown in figure 13(*e*) by sections E_1–E_1' and E_2–E_2', respectively. Shading represents the density field using the same color scale as figure 2. Arrows represent velocity vectors (u_2, u_3). Bold contour lines represent $\rho/\rho_0 = 1.005$ in (*a*) and $\rho/\rho_0 = 1.011$ in (*b*) and depict cross-stream plumes developing due to unstable stratification. Streamwise vorticity is shown by blue ($\omega_1/\omega_0 = 18$) and green ($\omega_1/\omega_0 = -18$) contour lines, similar to figure 6. Here d is the local depth at the slice.

figure 10, which depicts the x_2–x_3 slice shown in figure 9(*b*) over time. The strongest turbulence is seen in figure 10(*g*), after which the turbulence decays (figure 10*i*,*j*). Note that more lateral variability is generated as the downslope flow of dense water from the initial surge interacts with upslope flow under the next wave crest (figure 6*h*). This corresponds to the second, smaller peak in interior dissipation and mixing in figure 5(*a*), but is not seen in the slice shown in figure 10.

4.2. *Resolution requirements*

In order to resolve the turbulence that develops during wave breaking, certain grid-resolution requirements are placed on our simulations. First, we must resolve the large-scale sources of turbulence, including the shear stress created by the no-slip bottom boundary condition and regions of unstable stratification. Figure 11 shows vertical profiles of laterally averaged horizontal velocity u_1 and density ρ/ρ_0, where the vertical coordinate is shown in wall units $x_3^+ = x_3/\delta_S$ to emphasize the near-wall flow. Profiles are shown within the thin region of downslope flow between the interface and the bottom as the wave approaches the slope (figure 11*a*) and under the nose of the upslope surge (figure 11*b*). These examples were chosen to represent

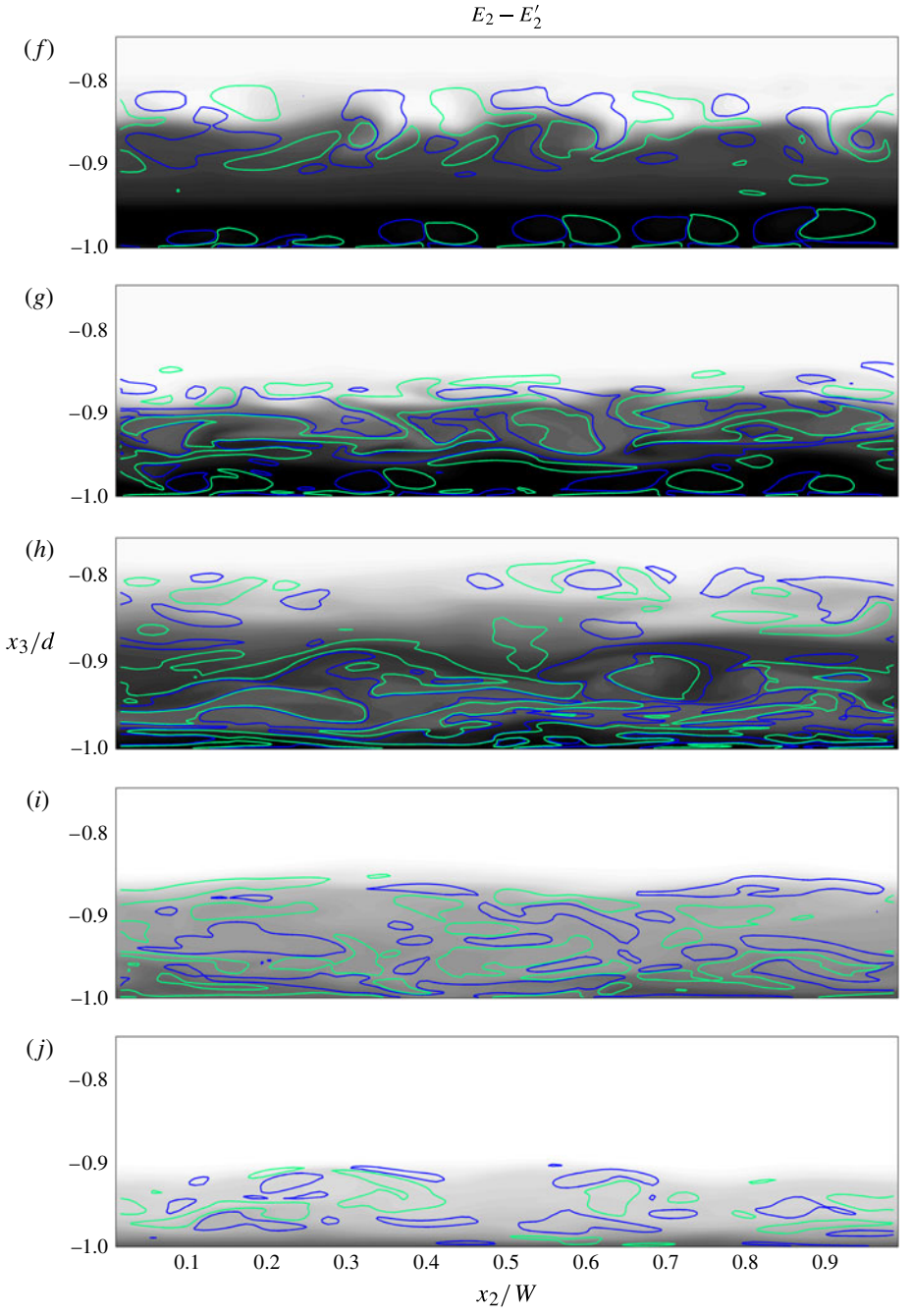

FIGURE 10. An x_2–x_3 slice through section E_2–E_2' in figure 13(*e*) at different time snapshots. Shading represents the density field using the same color scale as figure 2. Streamwise vorticity is shown by blue ($\omega_1/\omega_0 = 18$) and green ($\omega_1/\omega_0 = -18$) contour lines, as in figure 9. Here d is the local depth at the slice. Labels (*f*–*i*) correspond to the time snapshots from figures 2 and 6. Time point *j* is not shown in other figures, and corresponds to $t/T = 0.63$.

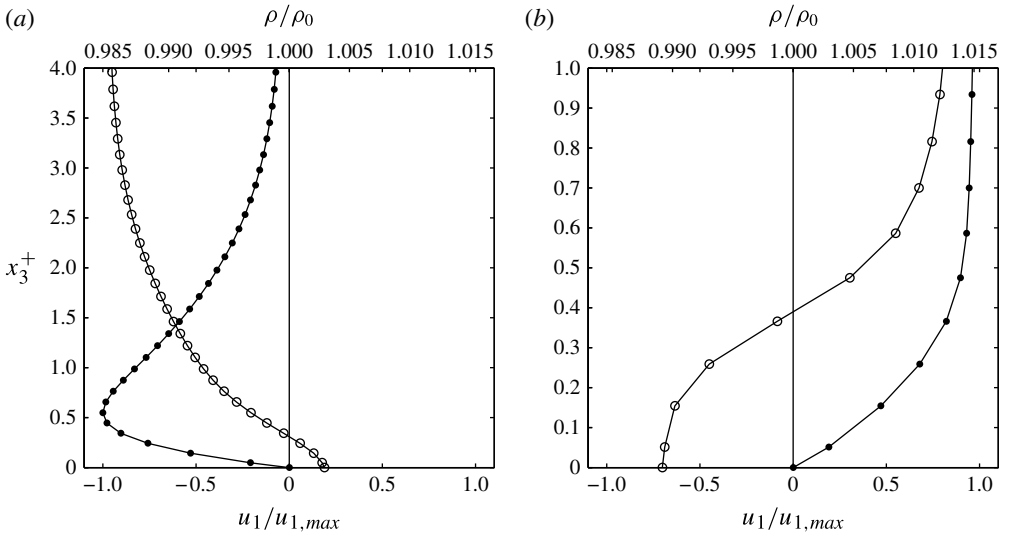

FIGURE 11. Vertical (x_3) profiles of laterally-averaged horizontal velocity u_1 (●) and density ρ/ρ_0 (○). (*a*) A vertical profile corresponding to section A–A' in figure 13(*a*). (*b*) A vertical profile corresponding to section E_2–E_2' (through the nose of the upslope surge) in figure 13(*e*). In both plots, u_1 is normalized by the maximum value over the full profile, and the vertical coordinate is shown in wall units $x_3^+ = x_3/\delta_S$ measured upward from the bottom. Note the difference in the range of the vertical axes.

extreme near-bottom gradients experienced during the simulations. It is clear in both cases that the flow near the bottom is well-resolved. By visual inspection, we also conclude that the initially two-dimensional (x_1–x_3) sources of unstable stratification are well-resolved in our domain.

In addition to resolving the large scales of the flow during wave breaking, resolving the turbulence cascade to smaller scales places an even stricter resolution requirement on our simulations. In order to demonstrate adequate resolution of the turbulence cascade, we define turbulence quantities as a departure from the lateral average. Specifically, $u_i = \overline{u}_i + u_i'$ where u_i is the full velocity, $\overline{u}_i$ is the laterally averaged velocity, and u_i' is the fluctuation about the lateral average. The density is decomposed in the same way, $\rho = \overline{\rho} + \rho'$. Figure 12 shows lateral spectra of the vertical velocity anomaly $E_{33}(k_2)$, where k_2 is the lateral wavenumber, for case 3 at four successive times after wave breaking has occurred. These spectra are averaged over the breaking region ($0.68 \leqslant x/L \leqslant 0.85$) in both the BBL (the bottom 10 vertical grid cells) and the interior ($40 \leqslant N_3 \leqslant 75$, which corresponds to $-0.93 \leqslant x_3/d \leqslant -0.81$ in figure 10). Results for the lateral spectra of the density anomaly ρ' in the same region are similar and are therefore not presented. Shortly after breaking, a spectral peak emerges in both the BBL and the interior at the observed wavenumber of the initial instability (see figure 9). This peak is clearly well resolved, with a normalized wavenumber of approximately 0.04. Over time, more broadband spectra are observed, with a cascade to smaller scales from the initial peak at the 'injection' scale. These results are comparable with those presented by Caulfield & Peltier (2000) (their figure 16) for DNS of stratified shear flow. While the development of turbulence in the BBL and the interior is similar, figure 12 shows that turbulence grows faster in the BBL, resulting in a fully turbulent spectrum at an earlier time. However, the overall magnitude of the

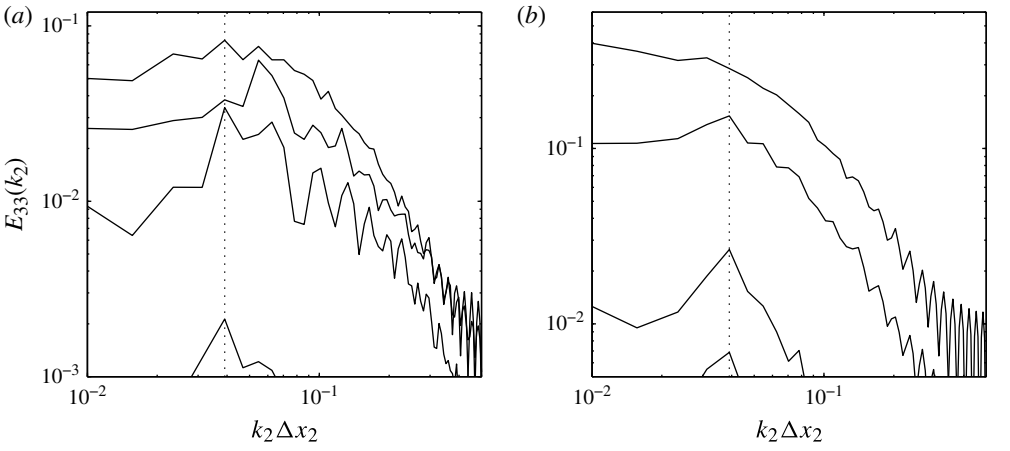

FIGURE 12. Lateral spectra of the vertical velocity anomaly $E_{33}(k_2)$ (in $\mathrm{m}^3\ \mathrm{s}^{-2}$) in both the BBL (*a*) and the interior (*b*). Spectra are shown at four successive times corresponding to snapshots (*d–g*) in figures 2 and 6. The observed wavenumber of the initial instability $(\cdots)$ is shown as well. The lateral wavenumber k_2 is normalized by the lateral grid spacing Δx_2.

turbulence is larger in the interior than in the BBL. Note that the magnitudes of the spectral peaks change with time due to the passing of the breaking wave through the averaging area and the resulting change in total turbulent kinetic energy. Ultimately, we must compare the grid resolution in our simulations to the Kolmogorov length scale, which we calculate here as $\eta_k = (\nu^3/\epsilon')^{1/4}$. The local turbulent dissipation is defined as

$$\epsilon' = 2\nu\overline{s'_{ij}s'_{ij}}, \tag{4.1}$$

where $s'_{ij} = ((\partial u'_i/\partial x_j) + (\partial u'_j/\partial x_i))/2$. We find that in the worst case scenario, the grid spacing is roughly one order of magnitude (a factor of 13) larger than η_k.

4.3. *Three-dimensionality*

As discussed in the previous section, our desire to accurately capture three-dimensional effects places a strict resolution requirement on the simulations. By comparing the three-dimensional results with those of a similar two-dimensional simulation, we can determine the relative importance of capturing these effects. Here, we present results from a two-dimensional version of breaking wave case 3 that differs from the three-dimensional version only in the number of lateral grid points, which is reduced from 96 to 1, suppressing lateral variability in the simulation. Figure 13 shows the density structure of the two-dimensional simulation (left column) and an x_1–x_3 slice through the centre of the three-dimensional simulation (right column) for comparison. The structure of the waves is essentially the same prior to breaking (figure 13*a,b*), and even during the breaking event and beginning of the upslope surge (figure 13*c,d*), before lateral variability develops in the three-dimensional simulation. However, as the billows at the interface evolve, the two-dimensional and three-dimensional results differ (figure 13*e–i*). Rather than breaking down due

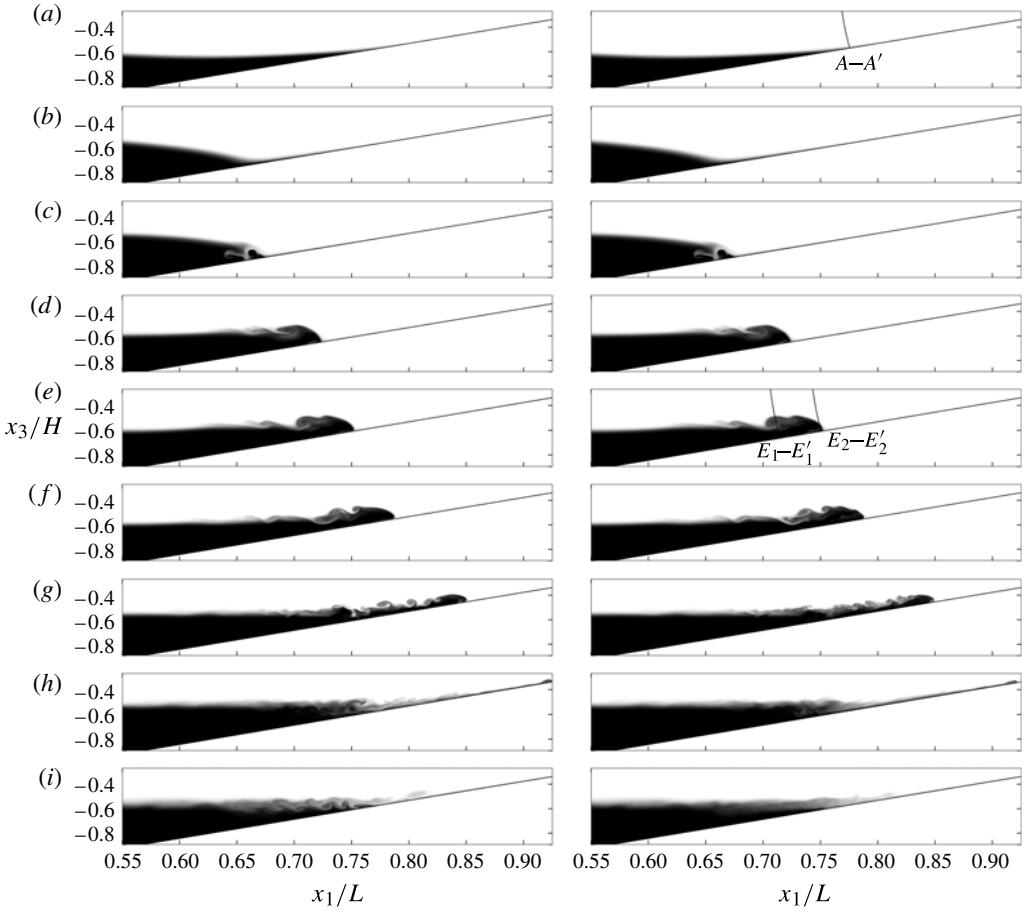

FIGURE 13. Snapshots in time of the density structure for two-dimensional (left column) and three-dimensional (right column) versions of breaking wave case 3 using the same colour scale as figure 2. The three-dimensional result is depicted by an x_1–x_3 slice through $x_2/W = 0.5$, the lateral centreline of the domain. Labels (*a–i*) correspond to the same times as in figures 2 and 6. The lines in panels (*a*) and (*e*), right column, are the locations of the x_2–x_3 slices shown in figures 9 and 10 and of the vertical (x_3) profiles shown in figure 11.

to lateral instability as they do in the three-dimensional simulation, the billows continue to grow and interact with one another, giving rise to the 'inverse energy cascade' of two-dimensional turbulence that is not realistic for a breaking internal wave. Similar differences were found by Aghsaee *et al.* (2012) when comparing their high-resolution two-dimensional numerical model results with the inherently three-dimensional laboratory experiments of Boegman *et al.* (2005).

Following Fringer & Street (2003), we can quantify the three-dimensionality introduced to the flow after the breaking event by partitioning the total kinetic energy E_k into its component parts

$$E_i = \frac{1}{2}\int_V u_i^2 \mathrm{d}V, \tag{4.2}$$

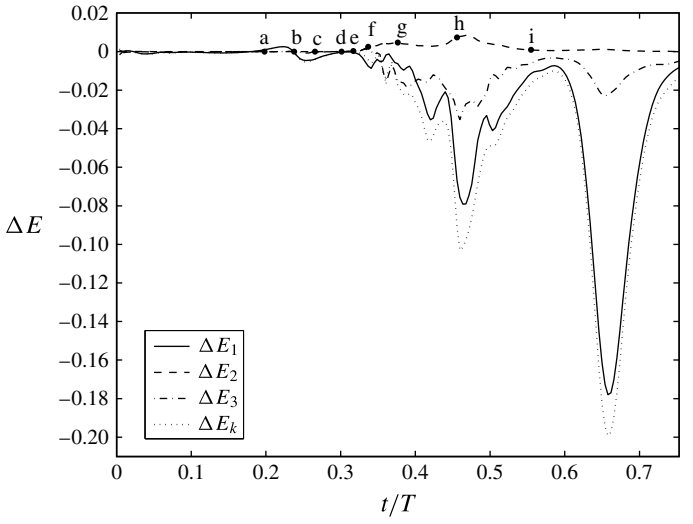

FIGURE 14. Normalized kinetic energy components quantifying the departure from two-dimensionality in breaking wave case 3. Shown are ΔE_1, ΔE_2, ΔE_3 and ΔE_k. Dots labelled a–i correspond to time snapshots from figures 2 and 6.

such that $E_k = E_1 + E_2 + E_3$. Here, V is the volume of the entire computational domain. The normalized departure from two-dimensionality is then given by

$$\Delta E_1 = \frac{E_{1,3} - E_{1,2}}{E_{k,3}}, \tag{4.3}$$

$$\Delta E_2 = \frac{E_{2,3}}{E_{k,3}}, \tag{4.4}$$

$$\Delta E_3 = \frac{E_{3,3} - E_{3,2}}{E_{k,3}}, \tag{4.5}$$

$$\Delta E_k = \frac{E_{k,3} - E_{k,2}}{E_{k,3}}, \tag{4.6}$$

where $E_{m,n}$ is the mth component of the kinetic energy from the n-dimensional computation and $E_{k,n}$ is the total kinetic energy of the n-dimensional computation. The results are presented in figure 14. During the time of elevated mixing (figure 14, points d–i), kinetic energy is transferred into the lateral (x_2) direction by the longitudinal rolls. Although only a small percentage of the total kinetic energy (a peak of approximately 1 % at $t/T = 0.47$) is contained in $E_{2,3}$, the total kinetic energy of the three-dimensional flow is 10 % less than that of the two-dimensional flow at this time. This value drops to nearly 20 % at $t/T = 0.66$ once the breaking event has completed.

The discrepancy between the kinetic energy in the two- and three-dimensional simulations can be attributed to the longitudinal rolls that are present and contribute to dissipation in the three-dimensional simulation, but are suppressed in the two-dimensional simulation. This is shown in figure 15, which presents the dissipation and mixing results for both simulations. Dissipation in the three-dimensional simulation ϵ_{3D} departs from the two-dimensional result ϵ_{2D} when the longitudinal rolls form (figure 15*a*, point d). Dissipation is then larger in the three-dimensional

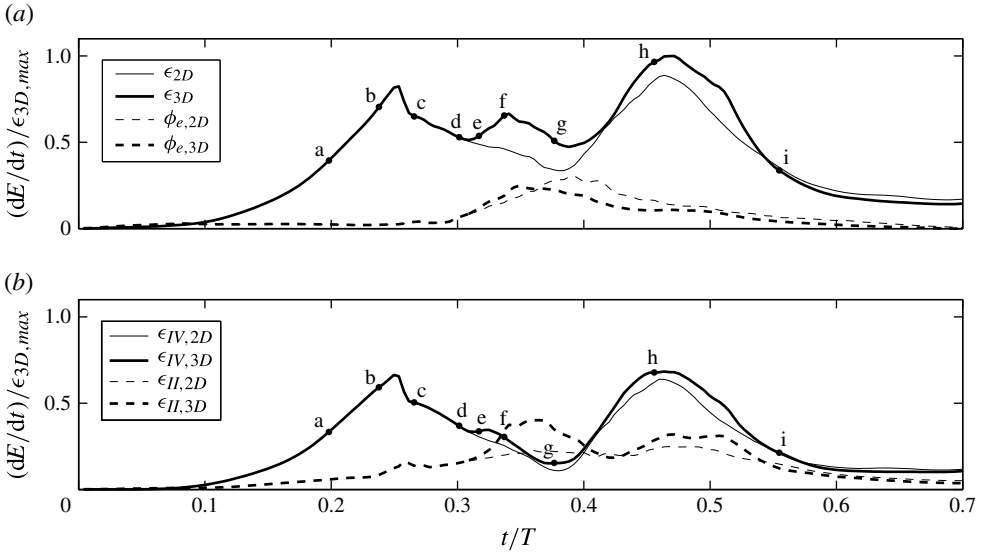

FIGURE 15. Dissipation and irreversible mixing for two- and three-dimensional versions of breaking wave case 3. (*a*) Dissipation for the two-dimensional case ϵ_{2D} and three-dimensional case ϵ_{3D}, as well as effective irreversible mixing for the two-dimensional case $\phi_{e,2D}$ and three-dimensional case $\phi_{e,3D}$. (*b*) The dissipation breakdown by region as defined in § 3.3, including dissipation in the bottom boundary region for the two-dimensional case $\epsilon_{2D,IV}$ and three-dimensional case $\epsilon_{3D,IV}$, as well as dissipation in the interior region for the two-dimensional case $\epsilon_{2D,II}$ and three-dimensional case $\epsilon_{3D,II}$. Both plots are normalized by the maximum dissipation in the three-dimensional simulation $\epsilon_{3D,max}$. Dots labelled a–i correspond to time snapshots from figures 2 and 6.

simulation throughout the breaking process, with a peak difference of roughly 30 % at $t/T = 0.36$ and a slightly smaller difference of roughly 25 % at $t/T = 0.51$. Figure 15(*b*) shows the dissipation breakdown between the interior and bottom boundary regions (as defined in § 3.3 and shown in figure 4) for both simulations as well. The peak difference in dissipation between the two- and three-dimensional results at $t/T = 0.36$ occurs predominantly in the interior region where $\epsilon_{3D,II}$ is nearly 50 % larger than $\epsilon_{2D,II}$. At $t/T = 0.51$, more comparable differences are seen in both the interior and bottom boundary regions; $\epsilon_{3D,II}$ is roughly 30 % larger than $\epsilon_{2D,II}$, while $\epsilon_{3D,IV}$ is roughly 20 % larger than $\epsilon_{2D,IV}$. Figure 15(*a*) also shows the effective irreversible mixing rate for the two-dimensional simulation $\phi_{e,2D}$ and the three-dimensional simulation $\phi_{e,3D}$. The peak mixing is higher in the two-dimensional simulation, and is larger throughout most of the breaking event, with a peak difference of roughly 30 % at $t/T = 0.42$. As discussed by Fringer & Street (2003), this increased mixing is attributed to the inverse energy cascade of two-dimensional turbulence. Because density overturns are not broken down by longitudinal rolls, they are able to grow and interact, creating sharper density gradients and increased surface area for interfacial diffusion. Overall, the three-dimensional simulation has roughly 8 % more dissipation and 20 % less mixing than the two-dimensional simulation, resulting in a 20 % smaller bulk mixing efficiency.

Owing to the effect of three-dimensional flow features (i.e. longitudinal rolls) on dissipation and mixing, a grid-resolution study was performed to ensure that our

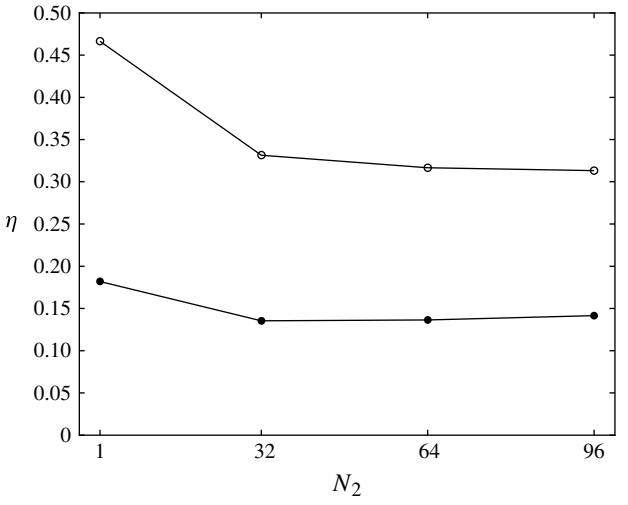

FIGURE 16. Maximum instantaneous mixing efficiency η_{max} (○) and bulk mixing efficiency η_B (●) as a function of the number of lateral grid points N_2 for breaking wave case 3. The x_1–x_3 grid and the domain width W are held constant.

energetics results are grid independent. Keeping the x_1–x_3 grid and domain width W constant, we varied the number of lateral grid points N_2 in order to better resolve the lateral variability discussed in § 4.1. Figure 16 shows the maximum instantaneous and bulk mixing efficiencies for case 3 as a function of N_2. As expected, both quantities are overestimated by the two-dimensional simulation ($N_2 = 1$). However, once lateral variability is resolved using a three-dimensional simulation, interior dissipation increases due to the presence of longitudinal rolls, and irreversible mixing decreases due to the lack of two-dimensional turbulence, leading to a decrease in mixing efficiency. The maximum instantaneous and bulk mixing efficiencies are relatively unaffected by increased lateral resolution for the three-dimensional grids tested. Both values have converged to the reported values of $\eta = 0.31$ and $\eta_B = 0.14$ for $N_2 = 96$, confirming that our results are grid independent.

5. Effects of wave amplitude and bathymetric slope

5.1. *General structure and energetics*

While the discussion of breaking wave case 3 in §§ 3 and 4 is generally applicable to all of the cases in table 1, several conditions may change the structure and energetics of the breaking process. Here, we consider the effects of initial wave amplitude a and bathymetric slope s on breaking dynamics. As shown in table 1, cases 1, 3, 4 and 5 have a constant bathymetric slope s, and thus vary only in the initial amplitude of the wave a. This results in different wave breaker types that are classified by Aghsaee *et al.* (2010). Figure 17 shows the density structure of breaking wave cases 1 (surging breaker) and 4 (plunging breaker) for comparison with case 3 (collapsing breaker). For smaller incoming waves, the rear face of the wave does not have enough momentum to overcome the downslope flow under the leading face, resulting in a relatively weak surging breaker (figure 17*a*). For larger waves, the rear face has enough momentum to plunge over the downslope flow under the leading face, resulting in a more vigorous

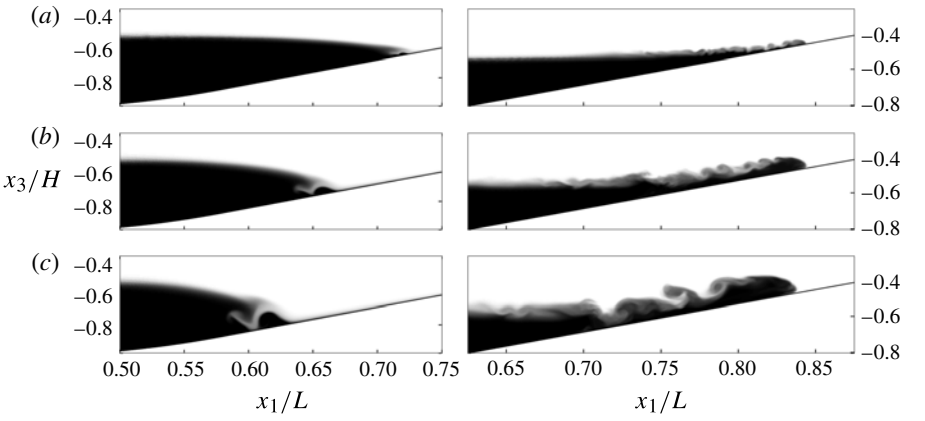

FIGURE 17. Snapshots in time of density structure for breaking wave cases 1, 3 and 4 just after the break point (left column), and during the upslope surge (right column). (*a*) Depicts case 1, a surging breaker, (*b*) depicts case 3, a collapsing breaker and (*c*) depicts case 4, a plunging breaker. Results are averaged in the lateral (x_2) direction.

plunging breaker (figure 17*c*). Case 3 represents a collapsing breaker (figure 17*b*), for which the rear face of the wave steepens, but is swept backward before it is able to plunge.

For a given bathymetric slope, the incoming wave amplitude has a clear effect on the energetics of the breaking process. While the shape of the energy profiles is similar for each case, the magnitudes are increased with increasing a. Furthermore, the dissipation breakdowns are similar in shape to that shown for case 3 in figure 5. That is, the dissipation is dominated by three peaks. The first and third peaks correspond to strong downslope flow in the bottom boundary region, first under the leading edge of the wave and then as dense water from the upslope surge recedes back downslope. The second peak in dissipation corresponds to the peaks in interior dissipation and irreversible mixing that are caused by density overturns and the formation of longitudinal rolls during breaking and the upslope surge.

Cases 2, 3, 6 and 7 have a constant amplitude a and are used to study the effect of varying bathymetric slope. The results for cases 2 ($s = 0.3$) and 6 ($s = 0.15$) are not shown due to their similarity with those of case 3 ($s = 0.218$) in figure 2. However, the structure and energetics of case 7 ($s = 0.05$) are significantly different than those of cases 1–6 because its low slope results in a fission breaker. Figure 18 shows snapshots in time of the density structure for case 7. Here, rather than breaking in the sense of a surging, collapsing, or plunging breaker, the initial solitary wave of depression disperses into a train of rank-ordered solitary waves of elevation (boluses) that propagate up the slope (figure 18*a,b*). The 'fission' occurs in figure 18(*c*), when a patch of dense fluid is pinched off of the leading wave of elevation, leading to density overturns at the interface. These density overturns interact with the trailing solitary waves as they propagate up the slope and eventually dissipate (figure 18*d–h*). This structure is strikingly similar to that shown in figure 3 of Helfrich (1992), which depicts experimental results with the same wave amplitude and bathymetric slope as case 7.

The dissipation breakdown for case 7 is shown in figure 19. Here, we see an almost entirely different energy profile than in cases 1, 3 and 6. Initially, dissipation rises due

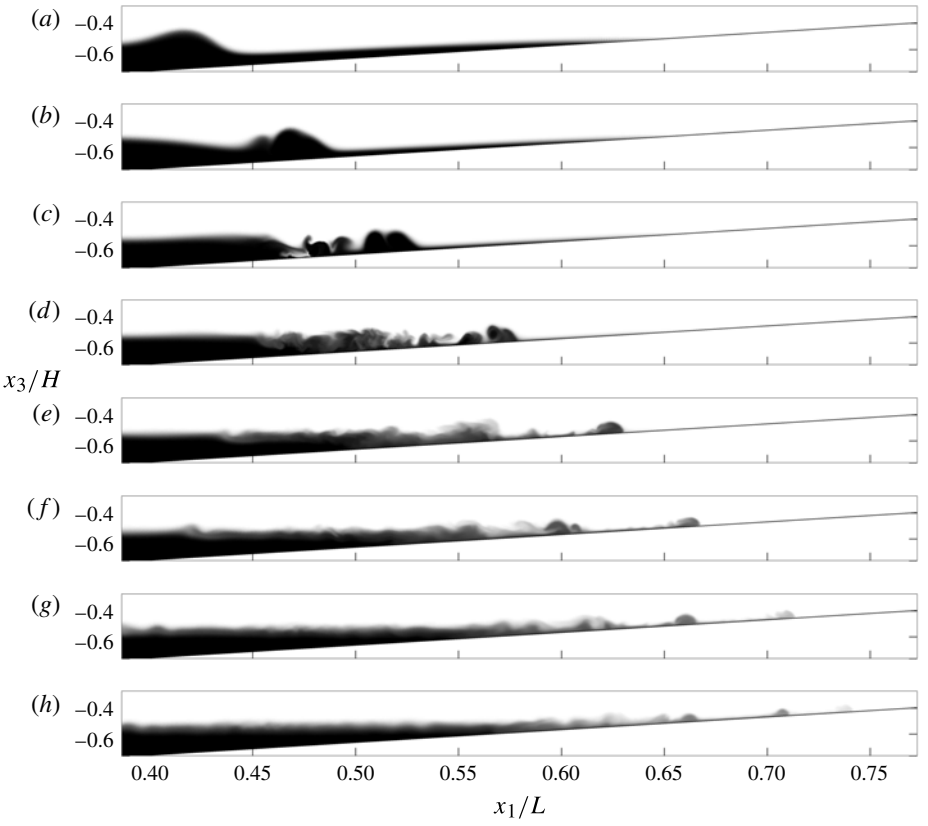

FIGURE 18. Snapshots in time of density structure for breaking wave case 7 using the same colour scale as figure 2. Results are averaged in the lateral (x_2) direction. Dots labelled (*a–h*) in figure 19 correspond to the labels shown here.

to downslope flow in the bottom-boundary region under the leading edge of the initial wave of depression (figure 19*a*, points a–c). The only major peak in dissipation and mixing occurs after the density overturns created by the fission event have had time to grow and spread along the interface (figure 19*a*, points c–d). After this peak, a lower level of dissipation and mixing is sustained as the train of solitary waves moves up the slope (figure 19*a*, points e–h), creating smaller density overturns along the interface. This corresponds to a sustained period of elevated instantaneous mixing efficiency. Helfrich (1992) also observed 'enhanced' mixing due to the runup of boluses after breaking. Although breaking occurs over a relatively longer period of time in case 7 than in cases 3 and 6, the cumulative percentages of bottom-boundary dissipation (60 %) and interior dissipation (36 %) are similar (figure 19*b*). We note that some dissipation (4 %) also occurs in the lower layer, which was not true for other cases (see figure 5), and accounts for the small gap between ϵ_{cum} and $\epsilon_{cum,II} + \epsilon_{cum,IV}$ in figure 19.

5.2. *Dissipation, mixing and mixing efficiency*

The combined effect of wave amplitude and bathymetric slope is described by the internal Iribarren number ξ, as defined in § 1. This parameter has been used in the

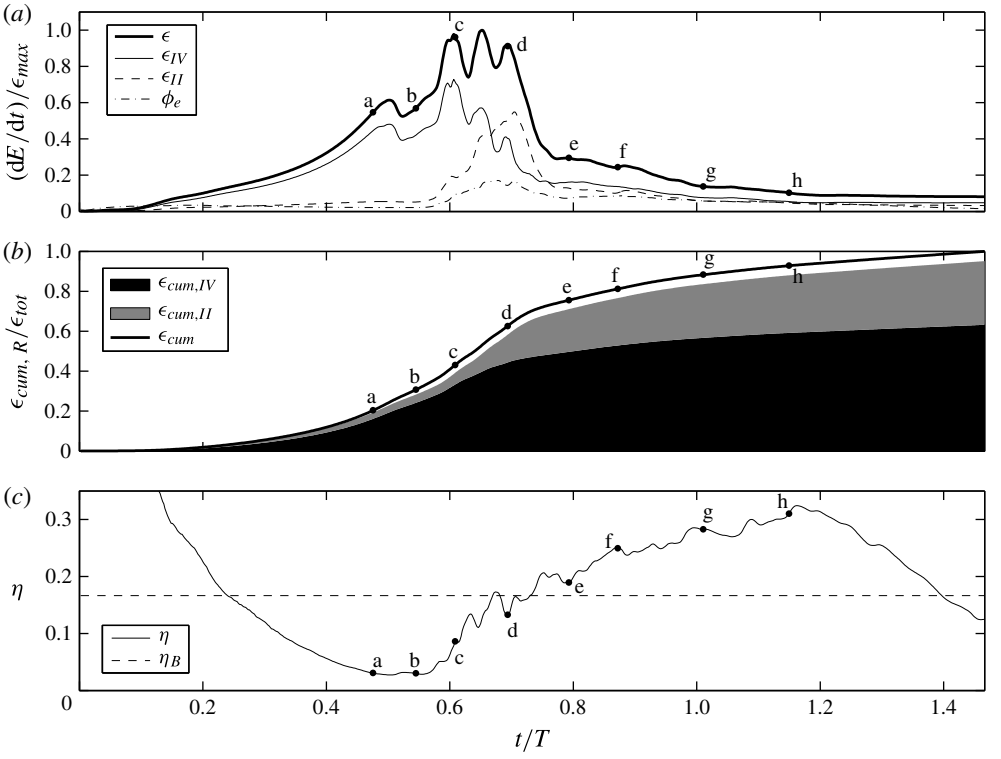

FIGURE 19. Dissipation breakdown by region and mixing efficiency for breaking wave case 7. (*a*) Total dissipation ϵ, bottom-boundary dissipation ϵ_{IV}, interior dissipation ϵ_{II}, and effective irreversible mixing ϕ_e as a function of time, all normalized by ϵ_{max}. (*b*) The cumulative dissipation in the bottom boundary region $\epsilon_{cum,IV}$ and in the interior region $\epsilon_{cum,II}$. The total cumulative dissipation ϵ_{cum} is shown as well. Values are normalized by ϵ_{tot}. (*c*) The instantaneous mixing efficiency η and bulk mixing efficiency η_B. Dots labelled a–h correspond to time snapshots from figure 18.

past to classify internal wave breaker types (Boegman *et al.* 2005; Aghsaee *et al.* 2010) and mixing efficiency (Boegman *et al.* 2005). Here, we consider the variation of dissipation, irreversible mixing and mixing efficiency with ξ, noting that Re_w is held constant in our simulations. Figure 20(*a,b*) shows peak and total values of dissipation and mixing as a function of the internal Iribarren number for all cases. We see a general decrease in dissipation and mixing with increasing ξ. However, a distinction exists between constant slope (varying amplitude) cases and constant amplitude (varying slope) cases. Both peak and total values of dissipation and mixing increase more rapidly with decreasing ξ for constant slope cases than for constant amplitude cases because larger amplitude waves have more initial energy to expend.

The mixing efficiency is a measure of the relative magnitudes of dissipation and mixing, and is plotted as a function of the internal Iribarren number in figure 20(*c*). Despite the decrease in both peak and total dissipation and mixing with increasing ξ, the bulk mixing efficiency does not follow this trend. Rather, η_B is found to increase for larger and smaller values of ξ, with a minimum for intermediate values of ξ and a spike around $\xi = 0.8$. We note that the peak instantaneous mixing efficiency (not shown) varies similarly between $\eta_{max} = 0.1$–0.4 with a spike of $\eta_{max} = 0.3$ around

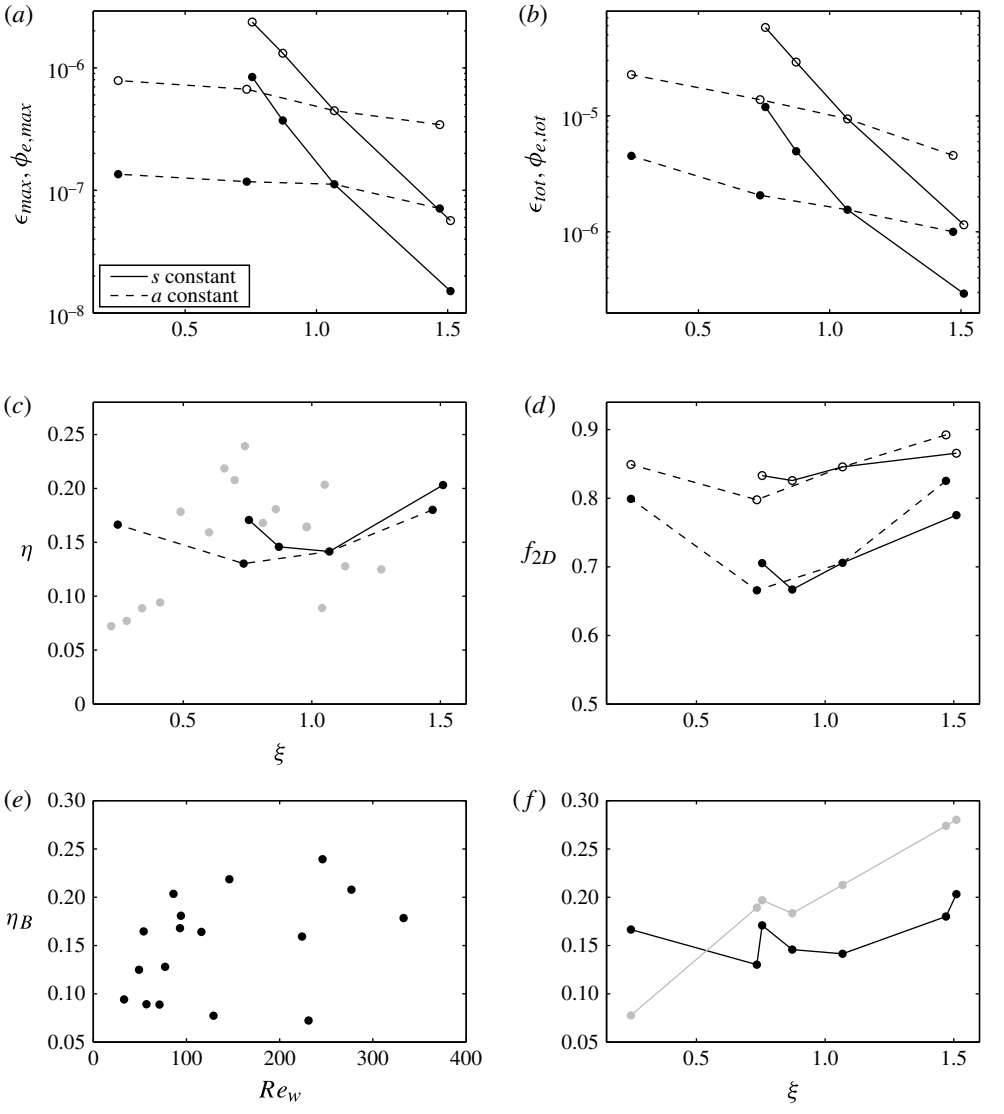

FIGURE 20. Dissipation, mixing and mixing efficiency results. (*a*) Peak and (*b*) total dissipation (○) and mixing (●) as functions of the internal Iribarren number ξ. (*c*) Bulk mixing efficiency (●) as a function of the internal Iribarren number ξ. The mixing efficiency results of Boegman *et al.* (2005) using the data of Michallet & Ivey (1999) are shown in grey for comparison. (*d*) The fraction f_{2D} of total dissipation (○) and mixing (●) accounted for by the laterally averaged flow as a function of the internal Iribarren number ξ. (*e*) Bulk mixing efficiency η_B versus wave Reynolds number Re_w for the data of Michallet & Ivey (1999). (*f*) Bulk mixing efficiency η_B as a function of internal Iribarren number ξ for our simulations (black) and interpolated from the data of Michallet & Ivey (1999) for $Re_w = 208$ (grey). In (*a*)–(*d*), constant slope (varying amplitude) cases 1, 3, 4 and 5 are connected with a solid line, while constant amplitude (varying slope) cases 2, 3, 6 and 7 are connected with a dashed line.

$\xi = 0.8$. Previous work by Boegman *et al.* (2005), using the data of Michallet & Ivey (1999), has shown that the bulk mixing efficiency η_B peaks around 0.25 for $\xi \approx 0.8$, and decreases for both larger and smaller ξ values. Their data is plotted in figure 20(*c*) for comparison. Although our values are similar, there is a discrepancy in the shape of the η_B versus ξ curve. Specifically, we see a minimum mixing efficiency, rather than a maximum, for intermediate Iribarren numbers, and we appear to overestimate mixing efficiency for both the largest and smallest Iribarren number case.

The discrepancy between our results and those of Michallet & Ivey (1999) and Boegman *et al.* (2005) can be explained by a Reynolds number (Re_w) effect. While we maintain a constant $Re_w = 208$ in our simulations and vary ξ, Michallet & Ivey (1999) varied Re_w and ξ simultaneously. Figure 20(*e*) shows Michallet & Ivey's (1999) mixing efficiency data as a function of Re_w, revealing that their mixing efficiency values generally increase with wave Reynolds number. In order to see how mixing efficiency varies strictly as a function of ξ, the effect of Re_w must be removed. Assuming $\eta_B = f(Re_w, \xi)$, we remove the Re_w effect from their data by creating an interpolant for η_B in Re_w–ξ space, and calculating η_B for a single value of Re_w. The result is shown in figure 20(*f*) for $Re_w = 208$ and compared with the seven values of ξ studied here. Accounting for Reynolds number effects in the laboratory data leads to a better agreement in the shape of the η_B versus ξ relationship with our results. Specifically, the bulk mixing efficiency from the experiments also peaks near $\xi = 0.8$ and increases for larger Iribarren numbers.

Although our results qualitatively agree with those of Michallet & Ivey (1999) when accounting for Reynolds number effects, a difference still exists for the lowest Iribarren number case, which has a larger mixing efficiency than the laboratory data. This is likely an effect of dissipation due to sidewall friction on the results of Michallet & Ivey (1999). Because Michallet & Ivey (1999) did not account for sidewall friction in their calculations, they overestimated the incident wave energy and underestimated the reflected wave energy off the slope (Bourgault & Kelley 2007*b*). This led to an overestimation of the total energy lost during breaking, and therefore an underestimation of mixing efficiency (see equation (12), Bourgault & Kelley 2007*b*). This effect was likely largest for the case with the lowest slope and therefore the longest distance over which sidewall dissipation could act. Because our computational domain does not have sidewalls (we use periodic boundary conditions in the lateral direction), sidewall dissipation does not affect our results, leading to a larger mixing efficiency for the lowest Iribarren number (lowest slope) case. The general difference in magnitude between our mixing efficiency results and those in the laboratory could occur for a number of reasons. In particular, we are unable to run our simulations until the waves come to rest as in the laboratory experiments because this would require a much larger domain and simulation time that would lead to computational requirements beyond our capabilities. Furthermore, unlike the laboratory experiments in which the mixing efficiency is computed with bulk energy changes, we calculate η_B using direct calculations of ϵ and ϕ_d. Finally, it is difficult to exactly match the initial stratification in the laboratory experiments.

For the low value of Re_w considered here, we find that the mixing efficiency is controlled by the two-dimensionality of the flow. This follows from the discussion in § 4.3, where we found a higher mixing efficiency for a two-dimensional simulation when compared with a similar three-dimensional simulation due to the suppression of longitudinal rolls. Along these lines, we would expect the mixing efficiency to depend on the degree of two-dimensionality in a given wave-breaking case. We quantify the two-dimensionality of the flow as the fraction f_{2D} of total dissipation or

mixing that is due to the laterally averaged flow. Thus, $f_{2D} = \overline{\epsilon}_{tot}/\epsilon_{tot}$ for dissipation and $f_{2D} = \overline{\phi}_{e,tot}/\phi_{e,tot}$ for mixing, where $\overline{\epsilon}$ is defined as in (3.9) but using the laterally averaged velocity $\overline{u}_i$ and $\overline{\phi}_e$ is defined with ϕ_d as in (3.5) but using the laterally averaged density $\overline{\rho}$. These quantities are displayed in figure 20(*d*), and show a similar dependence on ξ as η_B. It is clear that f_{2D} increases for larger and smaller values of ξ, with a minimum for intermediate values of ξ and a peak around $\xi = 0.8$. As in Boegman *et al.* (2005), the peak near $\xi = 0.8$ is due to the occurrence of plunging breakers, which introduce more available potential energy to the flow than collapsing breakers with similar internal Iribarren numbers. This also increases the two-dimensionality of the flow because the initial plunging motion does not vary in the lateral direction. Ultimately, a physical explanation of the dependence of mixing efficiency on two-dimensionality depends on the mechanisms of lateral instability during breaking, which are functions of Re_w, ξ and the non-dimensional interface thickness δ/λ.

6. Geophysical application

6.1. *Reynolds number effects*

The small spatial scale of the simulations presented here must be considered when assessing the geophysical relevance of the results. The present simulations can be related to geophysical flows using the turbulence activity number (or buoyancy Reynolds number) $Re_b = \epsilon'/\nu N^2$. This quantity can also be written as a ratio of the Ozmidov length scale $L_o = (\epsilon'/N^3)^{1/2}$ to the Kolmogorov length scale η_k as $L_o/\eta_k = Re_b^{3/4}$. Here, N is calculated conservatively using the initial stratification. A maximum Re_b of approximately two is reached for the current simulations, indicating a relatively small separation between the largest and smallest scales of turbulence. Based on the work of Shih *et al.* (2005), such a flow is classified in the 'diffusive' regime of stratified turbulence. Geophysical flows, on the other hand, usually have Re_b values that are one to many orders of magnitude higher, indicating a larger separation of scales. Such flows are classified in the 'intermediate' or 'energetic' regimes of stratified turbulence by Shih *et al.* (2005). Examples of Re_b calculations in the field include Davis & Monismith (2011), Walter *et al.* (2012) and Walter (2014) for nonlinear internal waves in the coastal environment, as well as (Bouffard & Boegman 2013, see figure 7) for the stratified region of Lake Erie.

The low Reynolds number of our simulations has several consequences for the interpretation of the results. In particular, dissipation in the boundary layer is much greater than that in the interior over the course of the wave-breaking event. For a higher-Reynolds-number flow, we would expect more energetic turbulence in the interior and therefore a larger relative contribution of the interior dissipation to the total dissipation. For example, in field observations of breaking internal waves in Monterey Bay, California, Walter *et al.* (2012) found dissipation values on the same order of magnitude in the interior as in the boundary layer. More energetic turbulence in the interior would also increase the turbulent contribution to the irreversible mixing ϕ_e, which in our simulations is roughly the same magnitude as the background mixing term ϕ_i. In addition, the boundary-layer dissipation in our simulations is largely due to the two-dimensional flow (figure 15*b*) because boundary-layer turbulence does not develop until after breaking and is confined to a small region. For a higher Reynolds number flow, we would expect more energetic turbulence to develop sooner in the boundary layer, that is, during the initial downslope flow under the leading edge of the wave in figure 2(*a*,*b*).

Aghsaee *et al.* (2010) considered the effect of Reynolds number on the internal wave-breaking mechanism, focusing on the scale of the boundary-layer instability that triggers breaking relative to the wave scale. They found that increasing the Reynolds number reduced both the relative size and growth rate of vortices shed from the boundary layer, thus reducing the effect of boundary-layer separation on wave breaking. This allowed the breaker type to change from collapsing to plunging (for the same internal Iribarren number) because the steepening rear face was no longer swept backwards by the separated downslope flow and was able to plunge forward. It is therefore likely that increasing the Reynolds number would also modify how the mixing efficiency of breaking internal waves varies with the internal Iribarren number, although the specific effect is unknown.

6.2. *Preturbulent mixing*

In addition to the effects described above, the Reynolds number also sets the relative contribution of preturbulent mixing to total mixing during the wave-breaking event. It is expected that as the Reynolds number increases, preturbulent mixing will contribute less to the total mixing because turbulent mixing will play a larger role. We demonstrate this by rerunning case 3 and increasing ν by factors of 2, 4 and 6 with $\kappa = \nu$ (thus reducing the Reynolds number by factors of 2, 4 and 6). Figure 21(*a*) shows total and laterally averaged irreversible mixing values for case 3 with the original viscosity and diffusivity $\nu_0 = \kappa_0 = 1 \times 10^{-6}$ m^2 s^{-1}, and with ν and κ increased by a factor of 4. Figure 21(*b*) shows the fraction of total mixing that occurs in the preturbulent stage as a function of κ, where the turbulent transition is defined as the point in time when ϕ_e departs from $\overline{\phi}_e$. Reducing the Reynolds number delays the onset of lateral variability during breaking. Thus, higher fractions of the peak and total mixing values are due to mixing in the preturbulent stage. We expect that increasing the Reynolds number of our simulations further would allow the turbulent transition to occur earlier in the shoaling and breaking event. This would likely reduce the large values of the mixing efficiency seen in figure 5 prior to breaking because the mixing efficiency would be less affected by preturbulent mixing. Extending our results to higher Reynolds numbers is the subject of future work.

6.3. *Local versus global energetics*

Despite the Reynolds number differences between geophysical flows and the flow simulated here, qualitative comparisons can still be made. To better relate the global (volume-integrated) energy quantities discussed thus far to what might be observed by a moored instrument during a breaking internal wave event in the field, we calculate local turbulence dissipation and buoyancy flux values at specific locations within the domain. Local turbulence quantities are defined as a departure from the lateral average as in § 4.2, and local turbulent dissipation ϵ' is defined as in (4.1). The local turbulent buoyancy flux is defined similarly as

$$b = \frac{g}{\rho_0}\overline{\rho' w'}. \tag{6.1}$$

Figure 22 shows the maximum local turbulent dissipation over the wave-breaking event for case 3. Turbulent dissipation is maximized after the breakpoint in the region of the upslope surge due to the presence of longitudinal rolls. Some turbulent dissipation is also evident offshore of the breakpoint due to the downslope return

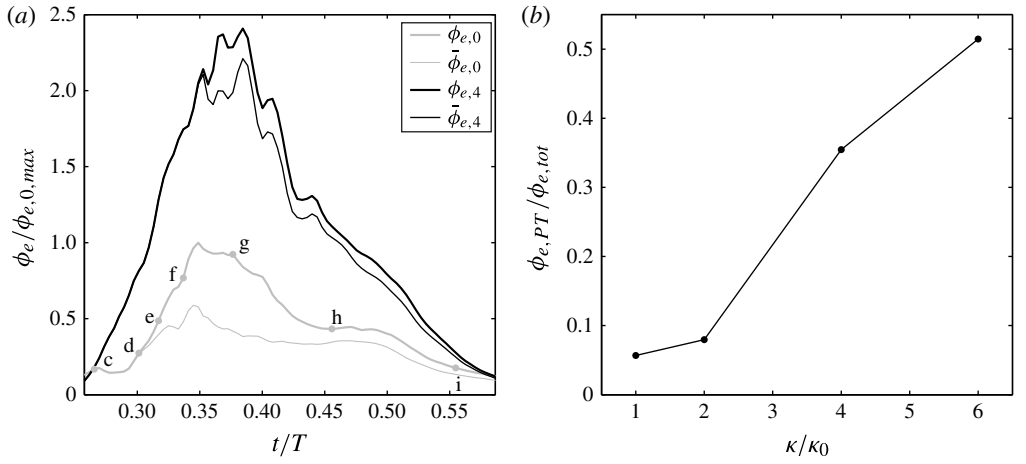

FIGURE 21. Irreversible mixing results for case 3 with increased viscosity ν and diffusivity $\kappa = \nu$ (lower Reynolds number). (*a*) Total and laterally averaged irreversible mixing values (ϕ_e and $\overline{\phi}_e$, respectively) for case 3 with the original viscosity and diffusivity $\nu_0 = \kappa_0 = 1 \times 10^{-6}$ m^2 s^{-1}, and with ν and κ increased by a factor of 4. Dots labelled c–i correspond to time snapshots from figures 2 and 6. (*b*) The fraction of total mixing that occurs in the preturbulent stage $\phi_{e,PT}/\phi_{e,tot}$ as a function of κ, where the turbulent transition is defined as the point in time when ϕ_e departs from $\overline{\phi}_e$.

flow after the upslope surge. Figures 23–25 show the density and velocity structure as well as turbulence quantities over time at the three cross-shore 'virtual mooring' locations in figure 22 for case 3, as would be measured at fixed moorings in the field. The density structure is depicted with a profile over time, while turbulence quantities are shown for two locations, one in the BBL (defined as the second grid cell from the bottom) and one in the interior (defined as the stratified region of the flow). These local results are presented in comparison with the global results for case 3, including ϵ, ϕ_e and $\int_V \epsilon' \mathrm{d}V$, the volume-integrated turbulent dissipation. Global quantities are divided by the volume of the sloping region of the domain to facilitate direct dimensional comparison with local quantities. The along-slope velocity at the boundary-layer measurement location $u_{s,BL}$ is also shown to relate energetics quantities to the phase of the flow. We do not distinguish between positive and negative values of b, only whether its absolute value is elevated above zero, indicating turbulent vertical transport of density. Furthermore, we do not calculate the local mixing efficiency because the flow is not in local equilibrium. This implies that some of the turbulent buoyancy flux is reversible and is therefore not a true measure of mixing.

Figures 23–25 show distinctly different signals depending on the cross-shore (x_1) location of the virtual mooring relative to the breakpoint of the wave and the vertical (x_3) location of the turbulence measurement. Furthermore, these local signals correspond to different parts of the global dissipation and mixing signal. The magnitudes of the strongest local turbulence signals are generally larger than the global signal. Specifically, the turbulent dissipation and buoyancy flux signals at M2 and M3 are between one and two orders of magnitude greater than the corresponding global signals. We are therefore concerned only with the shape of the turbulence signals, and do not attempt to relate them quantitatively to the global result. The

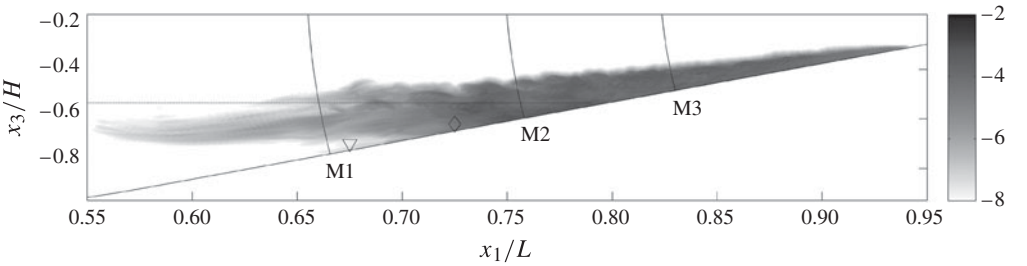

FIGURE 22. The locations of virtual moorings M1, M2 and M3 in figures 23–25, respectively. Included is the maximum (over the entire wave-breaking event) local turbulent dissipation $\epsilon'_{max}(x_1, x_3)$ (in m^2 s^{-3}) for breaking wave case 3 shown on a $\log_{10}$ scale, as well as the initial pycnocline (– –), the cross-shore location of the breakpoint ($\triangledown$) and the cross-shore location of the formation of the upslope surge ($\diamondsuit$).

magnitudes of the strongest local dissipation signals do, however, compare well with those observed in the laboratory by Hult *et al.* (2011) for breaking internal waves over a ridge, which are on the order of 10^{-4} or 10^{-5} m^2 s^{-3}. Owing to the difficulty of measuring local turbulent buoyancy flux in the laboratory, such values are not available for comparison (Hult *et al.* 2011).

Figure 23 shows the results from M1, which is located just downslope of the breakpoint. The density record shows the passage of a nonlinear wave prior to breaking. However, a relatively weak turbulence signal is seen here because most turbulence activity occurs upslope after breaking. A small spike in dissipation is seen in the boundary layer as the wave moves up the slope, and elevated dissipation and buoyancy flux are seen at the end of the event in the interior as dense water from the upslope surge flows back down the slope and interacts with the next wave crest. Figure 24 shows the results from M2, which is located upslope of the breakpoint and near the beginning of the upslope surge. Here, relatively strong signals are seen in both the BBL and the interior. Near the boundary, a peak in dissipation associated with the lobe–cleft instability at the front of the upslope surge is seen first. Then, a second peak is seen as dense water from the upslope surge flows back down the slope. In the interior, an extended period of elevated dissipation and buoyancy flux is seen after the upslope surge passes the mooring. This period is associated with the breakdown of billows at the interface due to lateral instability. These billows are evident in the density record in figure 24(*a*). A similar density structure was observed in the field by Walter *et al.* (2012, figure 4*a*) during the passage of an upslope propagating internal bore. The 'bores' in their study are the result of breaking internal waves on the nearshore slope in southern Monterey Bay, California. Figure 25 shows the results from M3, which is further up the slope. Here, we again see a relatively strong signal, but one that is different in shape than at M2. The density record shows the passage of the upslope surge; this is associated with peaks in dissipation both in the BBL and the interior, as well as elevated buoyancy flux in the interior.

The along-slope velocity at the boundary-layer measurement location was shown in figures 23(*b*), 24(*b*) and 25(*b*) in order to relate turbulent dissipation and buoyancy flux to the phase of the flow. At each virtual mooring, dissipation and buoyancy flux are enhanced at times of flow reversal from downslope (or zero flow) to upslope, specifically during the initial upslope surge of the breaking wave, and when the

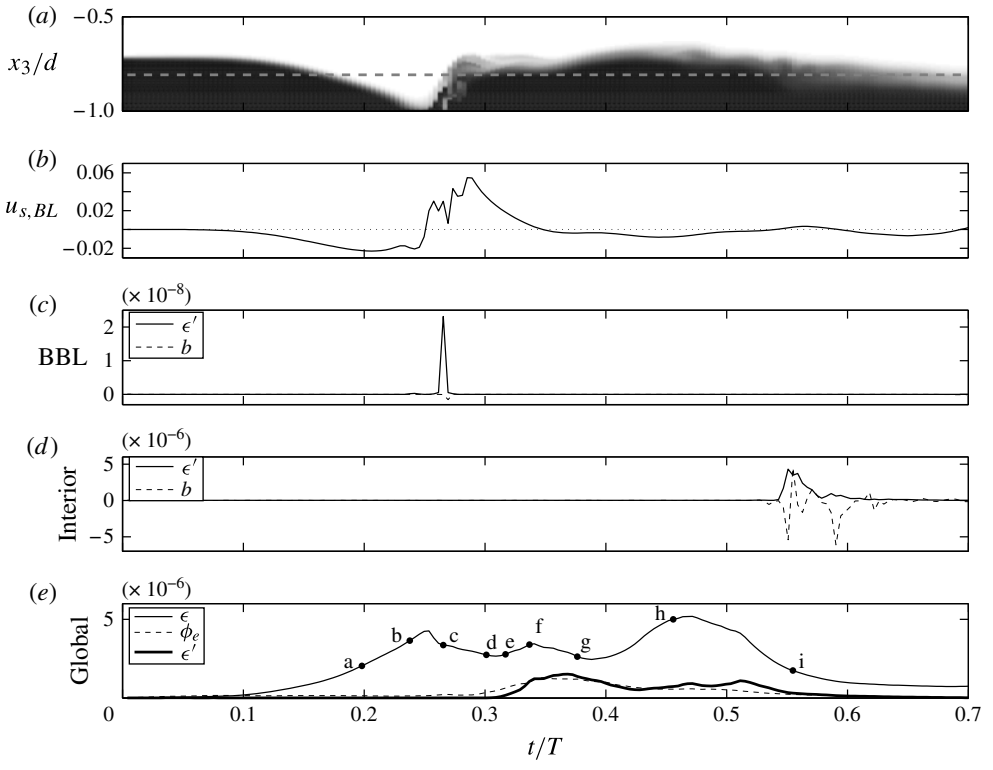

FIGURE 23. A comparison of local energetics to volume-integrated (global) energetics at $x/L = 0.67$ (M1 in figure 22) for case 3. (*a*) Density as a function of depth and time using the same colour scale as figure 2. (*b*) The along-slope velocity at the boundary-layer measurement location $u_{s,BL}$ (in m s^{-1}) as a function of time. (*c*) and (*d*) Local turbulent dissipation ϵ' and buoyancy flux b, both in m^2 s^{-3}, in the BBL region (*c*) and the interior region (*d*). The vertical location of the interior measurement is shown by a dotted line in (*a*). (*e*) Volume-integrated (global) dissipation ϵ, effective mixing rate ϕ_e, and turbulent dissipation $\int_V \epsilon' \mathrm{d}V$, all divided by the volume of the sloping region of the domain to give units of m^2 s^{-3}. Dots labelled a–i correspond to time snapshots from figures 2 and 6.

downslope flow from the upslope surge interacts with the next wave crest. Enhanced dissipation is also seen at mooring M2 during the downslope flow from the upslope surge. Similar trends were observed in the LES of Gayen & Sarkar (2011) and in the field observations of Aucan *et al.* (2006) at Kaena Ridge, Hawaii, both of which examined the phasing of near-bottom turbulence generated by internal tidal flow over a slope.

We acknowledge that the first peak in global dissipation in our simulations is attributed to laminar dissipation at the bottom boundary because turbulence has not yet developed. Therefore, this peak is not captured by the turbulence signal at any of the virtual moorings. This is evident in figures 23(*e*), 24(*e*) and 25(*e*), which show a time series of the global (volume-integrated) turbulent dissipation $\int_V \epsilon' \mathrm{d}V$. Turbulent dissipation does not develop anywhere in the domain until breaking occurs. It can also be noted that turbulent dissipation is absent near the bottom boundary offshore of the wave-breaking location in figure 22, which shows the maximum turbulent dissipation ϵ'_{max} over the course of breaking wave case 3 as a function of x_1

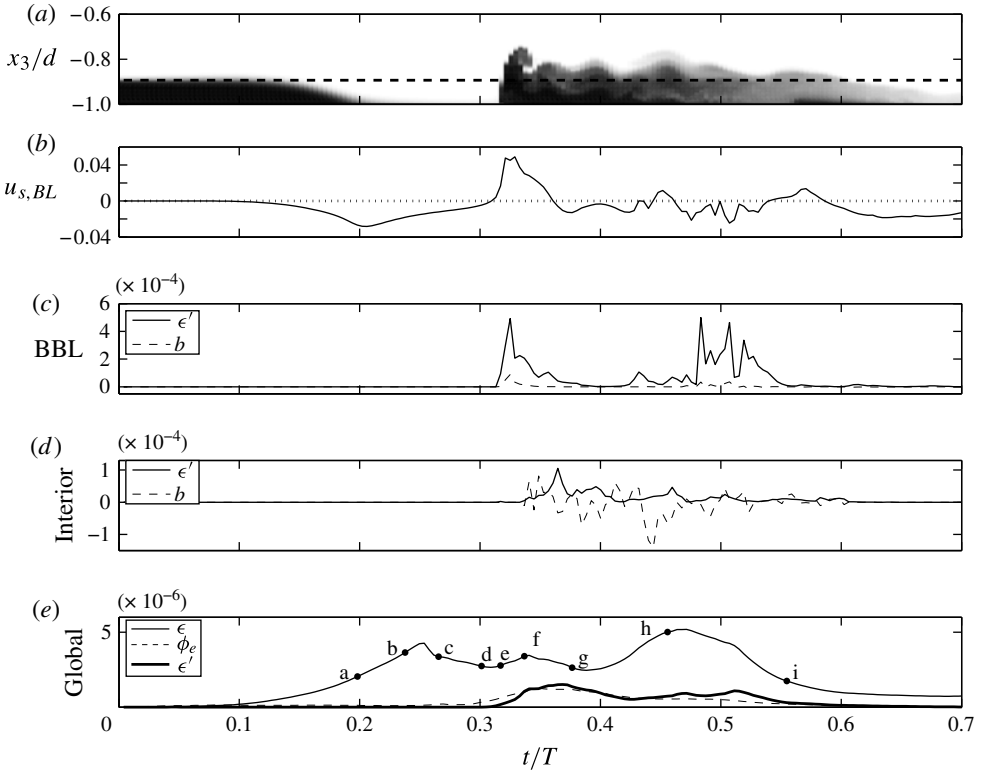

FIGURE 24. A comparison of local energetics to volume-integrated (global) energetics at $x/L = 0.76$ (M2 in figure 22) for case 3. (*a*) Density as a function of depth and time using the same colour scale as figure 2. (*b*) The along-slope velocity at the boundary-layer measurement location $u_{s,BL}$ (in m s^{-1}) as a function of time. (*c*) and (*c*) Local turbulent dissipation ϵ' and buoyancy flux b, both in m^2 s^{-3}, in the BBL region (*c*) and the interior region (*d*). The vertical location of the interior measurement is shown by a dotted line in (*a*). (*e*) Volume-integrated (global) dissipation ϵ, effective mixing rate ϕ_e, and turbulent dissipation $\int_V \epsilon' \mathrm{d}V$, all divided by the volume of the sloping region of the domain to give units of m^2 s^{-3}. Dots labelled a–i correspond to time snapshots from figures 2 and 6.

and x_3. In a higher-Reynolds-number flow, we would expect the first peak in global dissipation to also appear in the turbulent dissipation signal corresponding to the initial downslope flow under the leading edge of the wave. The turbulence signals seen at M1 and M2 would likely be modified to include this peak, while the signal at M3 would likely not change because of its position upslope of the initial density interface.

Comparison of local and global energetics allows us to determine which mooring location provides a signal that is most representative of the internal wave-breaking event as a whole. Through inspection of figures 23–25, we find that this is mooring M2, which is located offshore of the intersection of the initial pycnocline with the slope, and onshore of the breakpoint and formation of the upslope surge (see figure 22). Mooring M2 captures both peaks in dissipation after breaking; the first peak is due to the passing of the upslope surge, while the second peak is due to its return flow downslope. Furthermore, M2 captures elevated dissipation and buoyancy

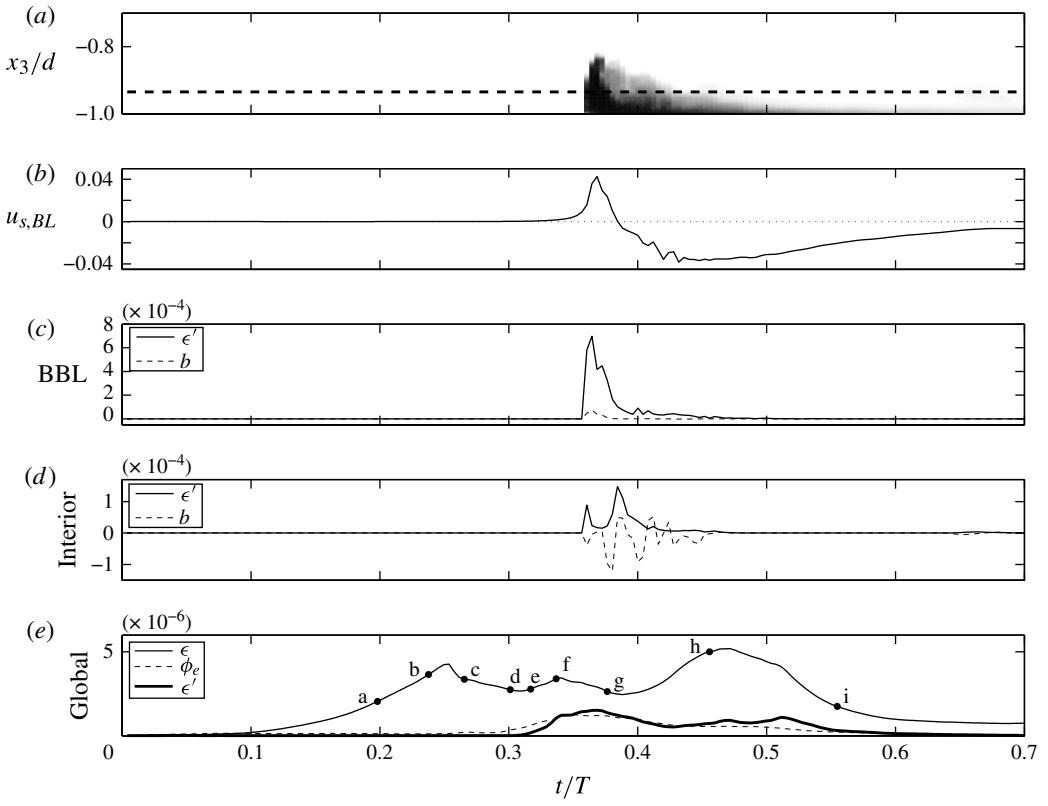

FIGURE 25. A comparison of local energetics to volume-integrated (global) energetics at $x/L = 0.83$ (M3 in figure 22) for case 3. (*a*) Shows density as a function of depth and time using the same color scale as figure 2. (*b*) Shows the along-slope velocity at the boundary layer measurement location $u_{s,BL}$ (in m s^{-1}) as a function of time. (*c,d*) Local turbulent dissipation ϵ' and buoyancy flux b, both in m^2 s^{-3}, in the BBL region (*c*) and the interior region (*d*). The vertical location of the interior measurement is shown by a dotted line in (*a*). (*e*) Volume-integrated (global) dissipation ϵ, effective mixing rate ϕ_e, and turbulent dissipation $\int_V \epsilon' \mathrm{d}V$, all divided by the volume of the sloping region of the domain to give units of m^2 s^{-3}. Dots labelled a–i correspond to time snapshots from figures 2 and 6.

flux in the interior associated with the breakdown of billows at the interface. In a more turbulent flow, M2 would likely also capture turbulent dissipation in the bottom boundary under the leading edge of the wave. From this single mooring location, one could potentially characterize dissipation and mixing for the entire breaking event. The same is not true for moorings M1 and M3. In the current simulations, mooring M1 is too far downslope to capture any relevant signal, although it would likely capture the initial peak in bottom-boundary dissipation in a more turbulent flow. Mooring M3 captures the upslope surge in both the bottom boundary and interior regions, but it is not representative of the event as a whole. These results imply that the cross-shore placement of field moorings relative to the breaking location and the vertical placement of instruments are critical to the interpretation of breaking internal wave observations.

7. Conclusion

Using DNS, we have simulated the three-dimensional structure of breaking internal solitary waves on slopes. Our study includes seven cases with varying initial wave amplitude, bathymetric slope, and internal Iribarren number, but constant wave Reynolds number. For each case, the structure and energetics of wave breaking were analysed, and wave energetics were separated into different regions of the flow. On average, bottom-boundary dissipation accounted for roughly 63 % of total dissipation in the domain, while the interior dissipation accounted for roughly 35 %. Peaks in dissipation were caused by strong shear due to downslope flow over the no-slip bottom boundary, as well as strong shear and density overturns at the interface during breaking and the upslope surge. Peaks in interior dissipation and irreversible mixing were found to correspond with three-dimensionality in the flow field associated with wave breaking. This three-dimensionality manifested itself in the form of a lateral (cross-stream) instability in two specific locations: the interface and the bottom. At the interface, unstable stratification was created by density overturns during breaking and the upslope surge, driving a cross-stream convective instability. At the bottom, unstable stratification was created under the nose of the upslope surge, which was raised above the no-slip bottom wall, leading to the lobe and cleft instability typical of gravity currents. Longitudinal rolls (streamwise vorticity) developed and grew from both of these sources, ultimately interacting to enhance interior dissipation and irreversible mixing. By comparing our results with those of a similar two-dimensional simulation, we quantified the effect of lateral variability on wave breaking. The two-dimensional simulation underestimated dissipation by as much as 30 % while overestimating irreversible mixing by as much as 30 %. Overall, the three-dimensional simulation had roughly 8 % more dissipation and 20 % less mixing than the two-dimensional simulation. These differences were attributed to the suppression of longitudinal rolls in the two-dimensional simulation and the inverse cascade of two-dimensional turbulence, respectively, and highlight the importance of capturing three-dimensional effects when considering the structure and energetics of breaking internal waves on slopes.

An additional goal of this study was to examine the variation in the structure and energetics of breaking internal waves with the initial amplitude of the wave and the bathymetric slope. The combined effect of these two parameters was considered in terms of the internal Iribarren number ξ. We found that both peak and total values of dissipation and irreversible mixing decrease with increasing ξ. However, the bulk mixing efficiency increases for larger and smaller values of ξ, with a minimum for intermediate values of ξ and a peak near $\xi = 0.8$ for plunging breakers. This trend was explained by the degree of two-dimensionality in the flow. Bulk mixing efficiency results were found to agree with those of Boegman *et al.* (2005) when the effect of Re_w was removed and the effect of sidewall friction was considered. Our results indicate that the mixing efficiency might be more appropriately classified as a function of both the wave slope and the bathymetric slope, as in Aghsaee *et al.*'s (2010) figure 6 for internal wave breaker types. It must be noted, however, that performing such a study using high-resolution, three-dimensional numerical simulations would require a great deal of computational effort.

Our average bulk mixing efficiency value of 0.16 and average peak instantaneous mixing efficiency value of 0.29 were found to be lower than Fringer & Street's (2003) averages of 0.42 and 0.36, respectively, likely due to the presence of the bottom boundary. However, our bulk mixing efficiency values were found to be slightly

higher than Hult *et al.*'s (2011) values of 0.04–0.07 because some boundary-driven turbulence contributed to the mixing in our domain, while boundary-driven turbulence was confined to the well-mixed bottom layer in their experiments.

Finally, we examined the geophysical application of our results and considered the effects of Reynolds number on dissipation and mixing. Specifically, we found that increasing the Reynolds number led to a decrease in preturbulent mixing. In order to better relate our volume-integrated results to what might be observed during a breaking internal wave event in the field, we also calculated local turbulent dissipation and buoyancy flux values for different 'virtual moorings'. We found distinctly different turbulence signals at each mooring, and showed that a mooring placed upslope of the breakpoint but downslope of the intersection of the pycnocline and the bottom provided results that were the most representative of dissipation and mixing over the event as a whole. This could assist in the interpretation of existing field measurements of breaking internal waves on slopes.

Acknowledgements

R.S.A. gratefully acknowledges the support of the Stanford Graduate Fellowship (SGF). R.S.A. and O.B.F. gratefully acknowledge the support of ONR grant N00014-08-1-0904 (scientific officers Dr C. Linwood Vincent, Dr T. Paluszkiewicz, and Dr S. Harper). We gratefully acknowledge the US Army Research Laboratory DoD Supercomputing Resource Center for computer time on Harold and especially thank the diligent staff at CCAC (Consolidated Customer Assistance Center) for their support. We also thank O. Murray of ONR for ensuring our access to these resources. Lastly, we thank three anonymous reviewers for their thoughtful and constructive comments that led to substantial improvement of the manuscript.

REFERENCES

AGHSAEE, P., BOEGMAN, L., DIAMESSIS, P. J. & LAMB, K. G. 2012 Boundary-layer-separation-driven vortex shedding beneath internal solitary waves of depression. *J. Fluid Mech.* **690**, 321–344.

AGHSAEE, P., BOEGMAN, L. & LAMB, K. G. 2010 Breaking of shoaling internal solitary waves. *J. Fluid Mech.* **659**, 289–317.

AUCAN, J., MERRIFIELD, M. A., LUTHER, D. S. & FLAMENT, P. 2006 Tidal mixing events on the deep flanks of Kaena Ridge, Hawaii. *J. Phys. Oceanogr.* **36** (6), 1202–1219.

BOEGMAN, L., IVEY, G. N. & IMBERGER, J. 2005 The degeneration of internal waves in lakes with sloping topography. *Limnol. Oceanogr.* **50** (5), 1620–1637.

BOUFFARD, D. & BOEGMAN, L. 2013 A diapycnal diffusivity model for stratified environmental flows. *Dyn. Atmos. Oceans* **61**, 14–34.

BOURGAULT, D., BLOKHINA, M. D., MIRSHAK, R. & KELLEY, D. E. 2007*a* Evolution of a shoaling internal solitary wavetrain. *Geophys. Res. Lett.* **34**, L03601.

BOURGAULT, D. & KELLEY, D. E. 2007*b* On the reflectance of uniform slopes for normally incident interfacial solitary waves. *J. Phys. Oceanogr.* **37** (5), 1156–1162.

BOURGAULT, D., MORSILLI, M., RICHARDS, C., NEUMEIER, U. & KELLEY, D. E. 2014 Sediment resuspension and nepheloid layers induced by long internal solitary waves shoaling orthogonally on uniform slopes. *Cont. Shelf Res.* **72**, 21–33.

CAULFIELD, C. P. & PELTIER, W. R. 2000 The anatomy of the mixing transition in homogeneous and stratified free shear layers. *J. Fluid Mech.* **413**, 1–47.

CHOU, Y. J. & FRINGER, O. B. 2010 A model for the simulation of coupled flow-bed form evolution in turbulent flows. *J. Geophys. Res.* **115**, C10041.

CUI, A. 1999 On the parallel computation of turbulent rotating stratified flows. PhD thesis, Stanford University.

DAVIS, K. A. & MONISMITH, S. G. 2011 The modification of bottom boundary layer turbulence and mixing by internal waves shoaling on a barrier reef. *J. Phys. Oceanogr.* **41** (11), 2223–2241.

DÖRNBRACK, A. 1998 Turbulent mixing by breaking gravity waves. *J. Fluid Mech.* **375**, 113–141.

FRINGER, O. B. 2003 Numerical simulations of breaking interfacial waves. PhD thesis, Stanford University.

FRINGER, O. B. & STREET, R. L. 2003 The dynamics of breaking progressive interfacial waves. *J. Fluid Mech.* **494**, 319–353.

GAYEN, B. & SARKAR, S. 2010 Turbulence during the generation of internal tide on a critical slope. *Phys. Rev. Lett.* **104** (21), 218502.

GAYEN, B. & SARKAR, S. 2011 Boundary mixing by density overturns in an internal tidal beam. *Geophys. Res. Lett.* **38** (14), L14608.

HÄRTEL, C., CARLSSON, F. & THUNBLOM, M. 2000 Analysis and direct numerical simulation of the flow at a gravity-current head. Part 2. The lobe-and-cleft instability. *J. Fluid Mech.* **418**, 213–229.

HELFRICH, K. R. 1992 Internal solitary wave breaking and run-up on a uniform slope. *J. Fluid Mech.* **243**, 133–154.

HELFRICH, K. R. & MELVILLE, W. K. 2006 Long nonlinear internal waves. *Annu. Rev. Fluid Mech.* **38**, 395–425.

HULT, E. L., TROY, C. D. & KOSEFF, J. R. 2011 The mixing efficiency of interfacial waves breaking at a ridge: 2. Local mixing processes. *J. Geophys. Res.* **116**, C02004.

KLYMAK, J. M. & MOUM, J. N. 2003 Internal solitary waves of elevation advancing on a shoaling shelf. *Geophys. Res. Lett.* **30** (20), 2045.

KOLTAKOV, S. & FRINGER, O. B. 2012 Moving grid method for numerical simulation of stratified flows. *Intl J. Numer. Meth. Fluids* **71** (12), 1524–1545.

LAMB, K. G. 2002 A numerical investigation of solitary internal waves with trapped cores formed via shoaling. *J. Fluid Mech.* **451**, 109–144.

LEICHTER, J. J., WING, S. R., MILLER, S. L. & DENNY, M. W. 1996 Pulsed delivery of subthermocline water to Conch Reef (Florida Keys) by internal tidal bores. *Limnol. Oceanogr.* **41** (7), 1490–1501.

LI, X., LU, P., SCHAEFFER, J., SHILLINGTON, J., WONG, P. S. & SHI, H. 1993 On the versatility of parallel sorting by regular sampling. *Parallel Comput.* **19** (10), 1079–1103.

MICHALLET, H. & IVEY, G. N. 1999 Experiments on mixing due to internal solitary waves breaking on uniform slopes. *J. Geophys. Res.* **104** (C6), 13467–13477.

MUNK, W. & WUNSCH, C. 1998 Abyssal recipes II: energetics of tidal and wind mixing. *Deep-Sea Res.* **45** (12), 1977–2010.

NAM, S. H. & SEND, U. 2011 Direct evidence of deep water intrusions onto the continental shelf via surging internal tides. *J. Geophys. Res.* **116**, C05004.

OMAND, M. M., LEICHTER, J. J., FRANKS, P. J., GUZA, R. T., LUCAS, A. J. & FEDDERSEN, F. 2011 Physical and biological processes underlying the sudden appearance of a red-tide surface patch in the nearshore. *Limnol. Oceanogr.* **56** (3), 787–801.

PINEDA, J. 1994 Internal tidal bores in the nearshore: warm-water fronts, seaward gravity currents and the onshore transport of neustonic larvae. *J. Mar. Res.* **52** (3), 427–458.

SCOTTI, A. & PINEDA, J. 2004 Observation of very large and steep internal waves of elevation near the Massachusetts coast. *Geophys. Res. Lett.* **31** (22), L22307.

SCOTTI, A. & WHITE, B. 2014 Diagnosing mixing in stratified turbulent flows with a locally defined available potential energy. *J. Fluid Mech.* **740**, 114–135.

SHIH, L. H., KOSEFF, J. R., IVEY, G. N. & FERZIGER, J. H. 2005 Parameterization of turbulent fluxes and scales using homogeneous sheared stably stratified turbulence simulations. *J. Fluid Mech.* **525**, 193–214.

SHROYER, E. L., MOUM, J. N. & NASH, J. D. 2009 Observations of polarity reversal in shoaling nonlinear internal waves. *J. Phys. Oceanogr.* **39** (3), 691–701.

SIMPSON, J. E. 1972 Effects of the lower boundary on the head of a gravity current. *J. Fluid Mech.* **53** (4), 759–768.

SMYTH, W. D. & WINTERS, K. B. 2003 Turbulence and mixing in Holmboe waves. *J. Phys. Oceanogr.* **33** (4), 694–711.

TROY, C. D. & KOSEFF, J. R. 2005 The instability and breaking of long internal waves. *J. Fluid Mech.* **543**, 107–136.

VENAYAGAMOORTHY, S. K. & FRINGER, O. B. 2007 On the formation and propagation of nonlinear internal boluses across a shelf break. *J. Fluid Mech.* **577**, 137–159.

VLASENKO, V. & HUTTER, K. 2002 Numerical experiments on the breaking of solitary internal waves over a slope-shelf topography. *J. Phys. Oceanogr.* **32** (6), 1779–1793.

VLASENKO, V. & STASHCHUK, N. 2007 Three-dimensional shoaling of large-amplitude internal waves. *J. Geophys. Res.* **112**, C11018.

WALLACE, B. C. & WILKINSON, D. L. 1988 Run-up of internal waves on a gentle slope in a two-layered system. *J. Fluid Mech.* **191**, 419–442.

WALTER, R. K. 2014 Nonlinear internal waves, internal bores, and turbulent mixing in the nearshore coastal environment. PhD thesis, Stanford University.

WALTER, R. K., WOODSON, C. B., ARTHUR, R. S., FRINGER, O. B. & MONISMITH, S. G. 2012 Nearshore internal bores and turbulent mixing in southern Monterey Bay. *J. Geophys. Res.* **117**, C07017.

WALTER, R. K., WOODSON, C. B., LEARY, P. R. & MONISMITH, S. G. 2014 Connecting wind-driven upwelling and offshore stratification to nearshore internal bores and oxygen variability. *J. Geophys. Res.* **116** (6), 3517–3534.

WINTERS, K. B. & D'ASARO, E. A. 1994 Three-dimensional wave instability near a critical level. *J. Fluid Mech.* **272**, 255–284.

WINTERS, K. B., LOMBARD, P. N., RILEY, J. J. & D'ASARO, E. A. 1995 Available potential energy and mixing in density-stratified fluids. *J. Fluid Mech.* **289**, 115–128.

ZANG, Y., STREET, R. L. & KOSEFF, J. R. 1993 A dynamic mixed subgrid-scale model and its application to turbulent recirculating flows. *Phys. Fluids* A **5** (12), 3186–3196.

ZANG, Y., STREET, R. L. & KOSEFF, J. R. 1994 A non-staggered grid, fractional step method for time-dependent incompressible Navier–Stokes equations in curvilinear coordinates. *J. Comput. Phys.* **114**, 18–33.